Waves of regulated protein expression and phosphorylation rewire the proteome to drive gametogenesis in budding yeast

Journal Article

Author(s):
Wettstein, Rahel; Hugener, Jannik; Gillet, Ludovic; Hernández-Armenta, Yi; Henggeler, Adrian; Xu, Jingwei; van Gerwen, Julian; Wollweber, Florian; Arter, Meret; Aebersold, Ruedi; Beltrao, Pedro; Pilhofer, Martin; Matos, Joao

Publication date:
2024-07-08

Permanent link:
https://doi.org/10.3929/ethz-b-000681707

Originally published in:
Developmental Cell 59(13), https://doi.org/10.1016/j.devcel.2024.05.025

CellPress
OPEN ACCESS

Developmental Cell

Resource

Waves of regulated protein expression and phosphorylation rewire the proteome to drive gametogenesis in budding yeast

Rahel Wettstein,[1,2,6] Jannik Hugener,[1,2,3,6] Ludovic Gillet,[4,6] Yi Hernández-Armenta,[5,6] Adrian Henggeler,[1,2] Jingwei Xu,[3] Julian van Gerwen,[4] Florian Wollweber,[3] Meret Arter,[2] Ruedi Aebersold,[4] Pedro Beltrao,[4,5,*] Martin Pilhofer,[3,*] and Joao Matos[1,2,7,*]

[1]Max Perutz Laboratories, University of Vienna, 1030 Vienna, Austria
[2]Institute of Biochemistry, ETH Zürich, 8093 Zürich, Switzerland
[3]Institute of Molecular Biology and Biophysics, ETH Zürich, 8093 Zürich, Switzerland
[4]Institute of Molecular Systems Biology, ETH Zürich, 8093 Zürich, Switzerland
[5]European Molecular Biology Laboratory, European Bioinformatics Institute (EMBL-EBI), Wellcome Genome Campus, Cambridge, UK
[6]These authors contributed equally
[7]Lead contact
*Correspondence: beltrao@imsb.biol.ethz.ch (P.B.), pilhofer@biol.ethz.ch (M.P.), joao.matos@maxperutzlabs.ac.at (J.M.)
https://doi.org/10.1016/j.devcel.2024.05.025

SUMMARY

Sexually reproducing eukaryotes employ a developmentally regulated cell division program—meiosis—to generate haploid gametes from diploid germ cells. To understand how gametes arise, we generated a proteomic census encompassing the entire meiotic program of budding yeast. We found that concerted waves of protein expression and phosphorylation modify nearly all cellular pathways to support meiotic entry, meiotic progression, and gamete morphogenesis. Leveraging this comprehensive resource, we pinpointed dynamic changes in mitochondrial components and showed that phosphorylation of the F_oF_1-ATP synthase complex is required for efficient gametogenesis. Furthermore, using cryoET as an orthogonal approach to visualize mitochondria, we uncovered highly ordered filament arrays of Ald4^{ALDH2}, a conserved aldehyde dehydrogenase that is highly expressed and phosphorylated during meiosis. Notably, phosphorylation-resistant mutants failed to accumulate filaments, suggesting that phosphorylation regulates context-specific Ald4^{ALDH2} polymerization. Overall, this proteomic census constitutes a broad resource to guide the exploration of the unique sequence of events underpinning gametogenesis.

INTRODUCTION

Sexual reproduction in eukaryotic organisms relies on meiosis, a developmentally regulated cell division program that halves the diploid genome of progenitor cells to generate haploid gametes.[1,2] To generate gametes, meiotic cells utilize general as well as dedicated molecular pathways that are different from those that drive the mitotic division of somatic cells. For example, the reductional segregation of homologous chromosomes during the first meiotic division requires a succession of specialized events, including the programmed breakage of chromosomes, the repair of broken chromosomes using crossover recombination, and the mono-orientation of sister kinetochores on the meiosis I spindle.[1] Each of these processes is vital to the success of meiosis but, at the same time, could be deleterious to cells undergoing meiosis II or a mitotic cell division. Therefore, meiosis requires a specialized cell-cycle program that orchestrates the orderly execution of events. Despite significant progress in recent years, we still lack a detailed molecular understanding—particularly at the post-translational level—of how meiotic cells modify the vast array of cellular pathways to control meiotic progression and enable the production of "healthy" gametes.

Gametogenesis also entails extensive cellular remodeling, encompassing structural and metabolic aspects.[3,4] Gametes are typically morphologically different from progenitor cells, as exemplified in mammals by motile sperm with flagella or by the enlarged oocytes.[5,6] Morphological changes are likewise prominent in unicellular organisms, such as budding yeast, which form four individualized spores within an ascus.[7] Spore formation relies on remodeling of the cellular architecture, including, among others, changes in cell size, cell envelope structure, and cytoplasmic composition.[8,9] Importantly, the viability and fitness of offspring depend not only on the appropriate inheritance of a haploid set of chromosomes by gametes but are also contingent on the controlled transmission of cytoplasmic macromolecules, biomolecular complexes, and entire organelles.[3,10–12] How cells modify and coordinate the plethora of specialized cellular processes that are required to form mature gametes remains poorly understood.

CellPress
OPEN ACCESS

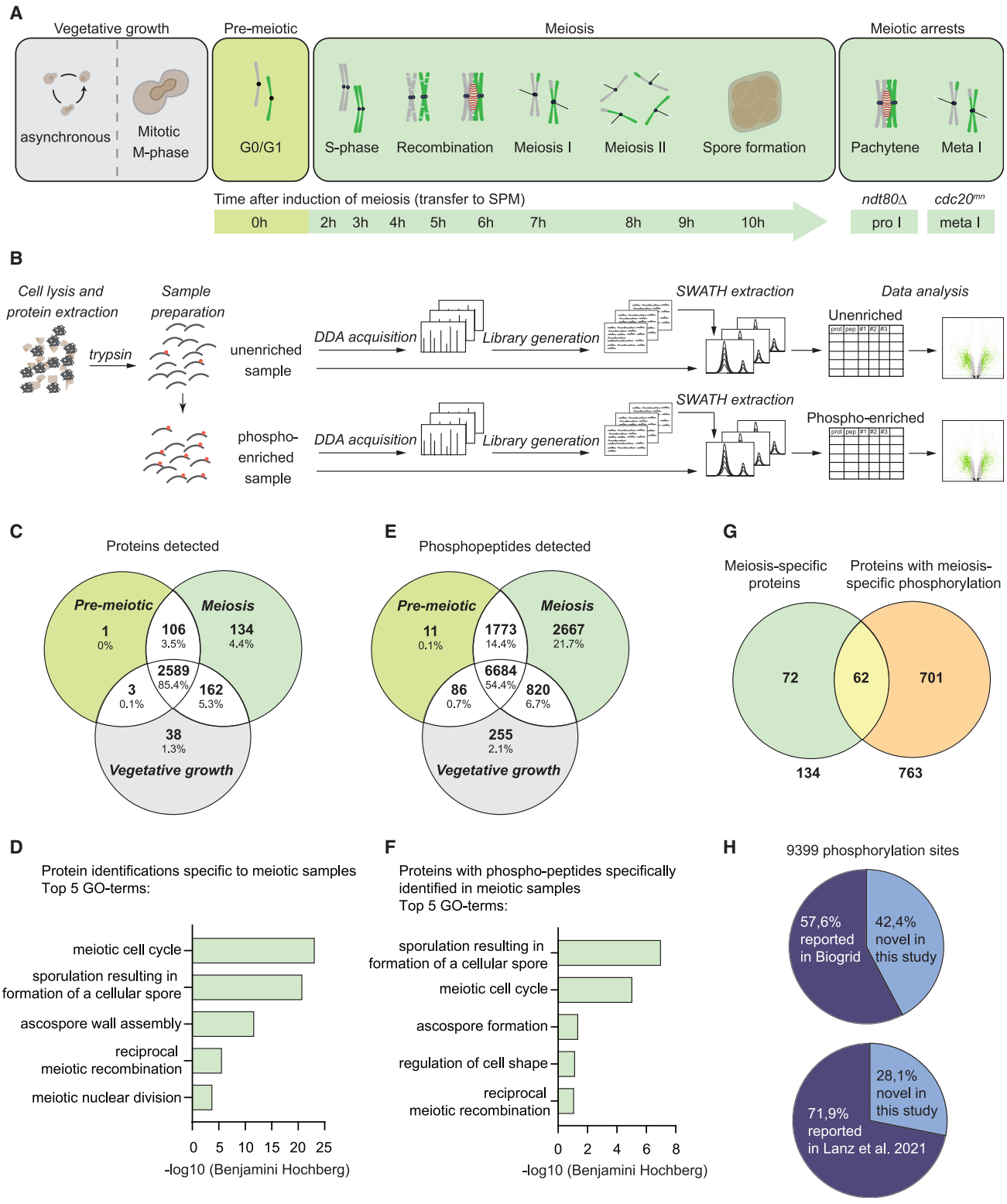

Figure 1. A census of meiotic protein expression and phosphorylation

(A) Experimental workflow and sampling strategy. Samples were collected from asynchronously proliferating (asynchronous) and nocodazole-synchronized mitotic cultures (mitotic M phase), representing vegetative growth. Meiotic samples were collected at regular time intervals after transfer of G0/G1 synchronized cultures (pre-meiotic G0/G1) to sporulation medium (SPM). Additional meiotic samples were collected from *ndt80Δ* and *cdc20*^{mn} mutants, which arrest meiotic

(legend continued on next page)

Viewed as a whole, gametogenesis is a meticulously orchestrated developmental program that requires numerous cellular events, unfolding across scales and following a precisely defined sequence. The induction of gametogenesis is itself tightly regulated and typically requires environmental cues for initiation.[13] In many unicellular organisms, including budding yeast, nutrient scarcity triggers gametogenesis/sporulation, which switches the metabolism from fermentation to mitochondrial respiration.[14,15] This adjustment is necessary to initiate the transcriptional cascade that regulates the commitment to meiotic entry, kick-starting the cell-cycle program that drives progression through meiosis and gamete morphogenesis.[4,14,16,17] Transcriptional and translational control of gene expression play important roles in broadly modifying the proteome of cells throughout meiosis.[17–19] However, the post-translational modification (PTM) of proteins—phosphorylation in particular—is thought to play major roles in coordinating the exquisite series of events driving gamete formation.[20–25] At least in part due to the lack of systems-level studies characterizing the precise targets and dynamics of protein phosphorylation throughout the whole process of gametogenesis, we remain far from understanding the full impact PTMs have on proteome rewiring.

Here, we have used sequential window acquisition of all theoretical mass spectra (SWATH-MS) to characterize changes in protein abundance and phosphorylation occurring throughout the entire meiotic program of budding yeast, from pre-meiotic G0/G1 to spore formation. We identified thousands of meiotic phosphorylation events and show that combined waves of regulated protein expression and phosphorylation rewire the proteome to support gametogenesis. Moreover, we verified the usefulness of the dataset as a hypothesis generator by deducing and validating roles for phosphorylation in the regulation of chromosome segregation, DNA repair, and mitochondrial respiration. Finally, prompted by Gene Ontology (GO) analyses of highly dynamic meiotic processes, we leveraged the proteomic census in combination with cryo-electron tomography (cryoET) to identify and characterize ordered protein filament arrays that assemble within mitochondria.

RESULTS

A meiotic census of protein expression and phosphorylation

To generate a comprehensive proteomic census covering all stages of meiosis, we synchronized diploid *S. cerevisiae* cultures at G0/G1 through the gradual starvation of vegetatively growing cells. Meiotic induction was then triggered by transfer of G0/G1 cells into sporulation medium (SPM), as previously described.[26,27] Samples were collected prior to the induction of meiosis and at 1 h intervals after transfer to SPM for 10 h (Figure 1A). To characterize meiotic progression, we followed the kinetics of several landmark events: DNA replication (Figure S1A), assembly and disassembly of the synaptonemal complex (SC) (Figure S1B), spindle morphology, and nuclear divisions in meiosis I and meiosis II (Figures S1B and S1C). Overall, in each of the three biological replicates, more than 95% of cells underwent meiotic nuclear divisions, and more than 80% of cells completed spore formation within the 10 h time courses (Figure S1C).

To characterize in greater depth prophase I and metaphase I, we performed similar experiments in the widely used meiotic mutants *ndt80Δ* and *cdc20^{mn}* (Figures 1A, S1A, S1D, and S1E).[29,30] As expected, *ndt80Δ* cells arrested meiotic progression with synapsed chromosomes in prophase I, and *cdc20^{mn}* mutants accumulated with a meiosis I spindle (Figures S1A, S1D, and S1E). Finally, to help identify potential meiosis-specific properties of the proteome, we also analyzed cells undergoing vegetative growth. We collected cells undergoing "asynchronous" exponential proliferation, in which a comparable proportion of the cells is in G1, S-phase, and G2/M (Figure S1F, top). In addition, to enrich for "mitotic M phase" cells, particularly useful for comparisons with meiotic *cdc20^{mn}* mutants, we treated the cultures with the microtubule depolymerizing drug nocodazole, which led to the accumulation of cells with a G2/M DNA content (Figure S1F, bottom).

Having obtained biological triplicates of the 14 samples (Figure 1A), we then prepared protein extracts that were processed for SWATH-MS proteomics (Figure 1B).[31–33] To enable the comprehensive detection of phosphorylated proteins, we also performed SWATH-MS analyses after a phosphopeptide enrichment step (Figure 1B). For simplicity, herein we refer to the two datasets as the "unenriched proteome" and the "phosphoproteome" (Figures S1G–S1J). Overall, for the unenriched proteome, we detected 25,122 unique peptides in the 42 samples analyzed (Figure S1K). The peptides could be assigned to 3,033 proteins, accounting for ~52% of the predicted budding yeast proteome[34] (Figure S1K). After phospho-enrichment, we detected 12,296 unique phosphopeptides, originating from 1,875 proteins and covering 32% of the proteome (Figure S1K).

progression in prophase I (pachytene) and metaphase I (meta I), respectively. Samples from *ndt80Δ* and *cdc20^{mn}* strains were collected 8 and 10 h after induction of meiosis, respectively. All samples were prepared in biological triplicates.

(B) Sample processing strategy and bioinformatics pipeline to characterize the proteome of cells prepared as described in (A) by SWATH-MS proteomics. See STAR Methods for details.

(C) Venn diagram with overlapping and non-overlapping protein identifications in pre-meiotic, meiotic, or cells undergoing vegetative growth, as color-coded in (A).

(D) Gene Ontology (GO) analysis of proteins identified specifically in meiotic samples from (C). The top 5 scoring GO terms are shown. *p* values are corrected for multiple testing (Benjamini-Hochberg) and $-\log_{10}$ transformed. The full list of GO terms is available in Table S1.

(E) As in (C) for phosphopeptides.

(F) As in (D) for all proteins with phosphopeptides detected specifically in meiotic cells. The top 5 scoring GO terms are shown. *p* values are corrected for multiple testing (Benjamini-Hochberg) and $-\log_{10}$ transformed. The full list of GO terms is available in Table S1.

(G) Venn diagram depicting the number of proteins that are specifically detected in meiosis or that have phosphopeptides that are specifically detected in meiosis.

(H) Pie chart depicting the phosphosites identified in this study, the BioGrid phospho-repository or Lanz et al,[28] respectively. Only S, T, and Y phosphorylations were considered.

See also Figure S1 and Table S1.

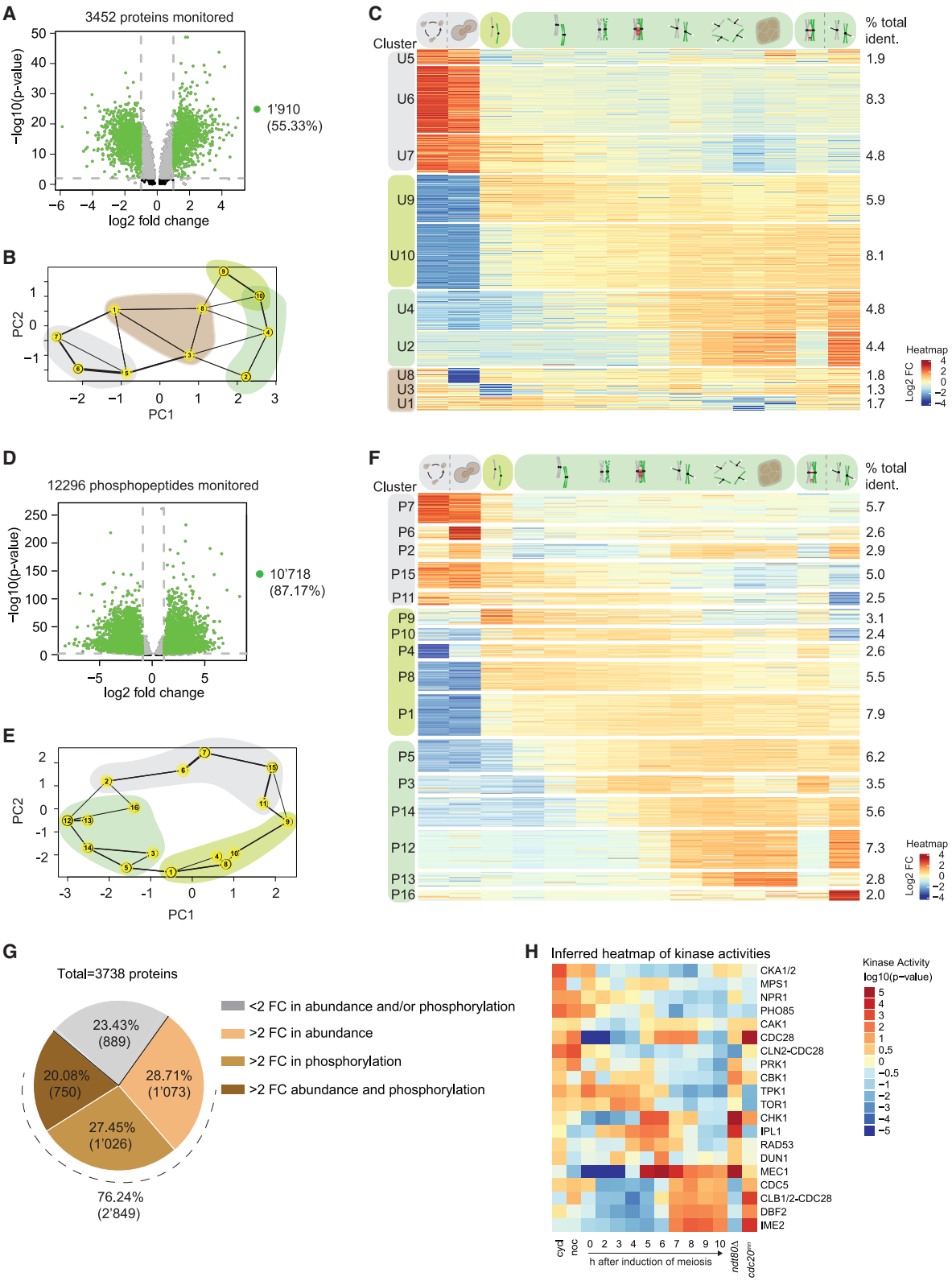

(legend on next page)

When combining the two datasets, we reached a total of 3,738 proteins, indicating that at least 64% of the predicted yeast proteome is expressed in the cellular contexts analyzed.

Thousands of protein phosphorylation events during meiosis

To identify context-specific proteins and phosphorylation events, we cross-compared the identities of proteins/phosphopeptides found in meiotic cells, pre-meiotic G0/G1, and vegetative growth. More than 85% (2,589) of the proteins in the unenriched proteome were common to all three cellular contexts, with just 4.4% (134 proteins) being exclusively detected in cells undergoing meiosis and 1.3% (38 proteins) in cells undergoing vegetative growth (Figure 1C; Table S1). We note that the inability to detect a protein/peptide in a given cellular context does not necessarily imply its absence, since the expression level of some proteins may fall below the detection limits of SWATH-MS. Nonetheless, GO enrichment analyses of the proteins that were specifically detected in meiotic cells showed a marked enrichment for meiosis-specific processes, such as "meiotic cell cycle," "meiotic nuclear divisions," and "sporulation" (Figure 1D), providing confidence in the overall strategy employed.

A much higher proportion (21.7%) of the identified phosphopeptides was specific to the meiotic samples (Figure 1E). Since proteins with meiosis-specific phosphopeptides were also strongly associated with meiotic processes (Figure 1F), we asked if their expression tended to be meiosis-specific. Interestingly, just 62 of the 763 proteins with meiosis-specific phosphopeptides were detected exclusively in meiotic cells (Figure 1G; Table S1). This suggests that most meiosis-specific phosphorylation occurs in proteins that are also expressed in other cellular contexts or ubiquitously (Figure 1G).

Since the entire meiotic program was not analyzed in previous phosphoproteomic studies and given the large number of phosphopeptides detected exclusively in these two contexts (4,451 phosphopeptides) (Figure 1E), we anticipated the identification of previously unknown phosphorylation sites. To test for this possibility, we performed a phosphorylation site localization analysis[33,35] and obtained a total of 9,399 putatively modified serine, threonine, or tyrosine (S/T/Y) residues. The proportion of S/T/Y phosphorylation was similar to the one observed in previous reports (Figure S1L; Table S1). However, 42.4% of the sites identified were not previously reported in the BioGrid repository,[36] and 28.1% were not annotated in a recent resource that consolidated 75 previous independent proteomic studies[28] (Figure 1H). These data suggest that meiosis-specific phosphorylation plays a broad role in shaping the proteome to support the specialized requirements of gametogenesis.

Sequential waves of protein expression and phosphorylation throughout gametogenesis

To gain more detailed insight into how cells rewire the proteome during gametogenesis, we took advantage of the time series to identify proteins that display dynamic changes in expression and/or phosphorylation (Figure 1A). 55.3% of the proteins detected in the unenriched proteome showed a >2-fold change in abundance in at least one of the fourteen cellular contexts studied (Figure 2A). Within this subset, we identified ten expression clusters (U1–U10),[38] which could be subdivided into four broad groups: proteins with overall higher expression levels in cells undergoing vegetative growth (gray); proteins with high expression in pre-meiotic G0/G1 and throughout meiosis (olive green); proteins with increased expression specifically during meiosis (green); proteins with lower expression in very specific cellular contexts (brown) (Figures 2B and 2C; Table S2). While exploring the phosphoproteome dataset, we noticed that a significantly higher fraction (87.17%) of the phosphopeptides showed a >2-fold change in abundance (Figure 2D). Even though we did observe similar expression pattern groups when comparing

Figure 2. Sequential waves of regulated protein phosphorylation during gametogenesis

(A) The relative abundance of 3,452 proteins detected in Figure 1A, at each time point, was determined and compared with the average expression level of that same protein across all samples analyzed. The resulting $\log_2$ fold changes (FC) were analyzed by ANOVA testing and volcano plotted. Significance cutoff is FC > 2 and $p < 0.01$ (after correction for multiple comparisons). Significant values are shown in green.

(B) Principal component (PC) analysis of fuzzy clustering of significant output from (A). Graph shows the relationship between individual clusters. Line thickness between nodes corresponds to degree of overlap between two clusters. Colors highlight further similarities between clusters in the inferred overall temporal order in protein expression shown in (C).

(C) Heatmap of significant values from (A) grouped in clusters according to (B). Red signifies upregulated, and blue downregulated protein abundance. $\log_2$ FC > 4 or < −4 are capped. Cluster numbers are assigned randomly. Preceding "U" stands for unenriched proteome. The clusters have been arranged according to the pseudo-temporal peak of expression. Colors on the left column and top scheme highlight further similarities: gray, predominant expression in mitotically dividing cells; olive green, increased expression in pre-meiotic G0/G1 and throughout meiosis; green, meiosis-specific increase in expression; brown, depleted in specific cellular contexts. Numbers in the right column indicate the fraction (%) of proteins associated with each cluster. Note: proteins that change in abundance but do not cluster are not shown.

(D) Volcano plot as in (A) for the phosphoproteome data.

(E) Principal component analysis of fuzzy clustering, as in (B), for the significant output from (D).

(F) Heatmap of significant values from (D) grouped in clusters according to (E). $\log_2$ FC > 4 or < −4 are capped. Cluster numbers are assigned randomly. Preceding "P" stands for phosphoproteome. The clusters have been arranged according to the pseudo-temporal peak of expression. Color-coded as in (C). Numbers in the right column indicate the fraction (%) of phosphopeptides associated with each cluster. Note: phosphopeptides that change in abundance but do not cluster are not shown.

(G) Pie chart depicting the fraction of detected proteins with >2 FC in abundance only (orange), phosphorylation only (light brown), abundance and phosphorylation (dark brown), or neither (gray).

(H) Inferred heatmap of kinase activities. Complex heatmap showing the kinase activity inferred from characterized kinase targets[37] in the phosphoproteome dataset across all samples analyzed. Red signifies a relative increase in kinase activity, blue a decrease. Coordinated changes in kinase activity (abs(log10(p value)) ≥ 1) are observed from early to late time points of meiotic progression. A complete list of kinase targets including the scoring proteins can be found in Table S3.

See also Figure S2 and Tables S2 and S3.

phosphopeptides and proteins, the number of phosphopeptide clusters in pre-meiotic (olive) and meiotic (green) cells was significantly higher (11 vs. 4) (Figures 2B, 2C, 2E, and 2F, note color code).

To estimate the contribution of changes in protein abundance to the dynamics of protein phosphorylation, we focused on a subset of 1,169 proteins that were reliably detected in both the unenriched proteome and the phosphoproteome (Figure S2A). After correcting the expression pattern of each phosphopeptide based on the relative abundance of the respective protein, we found that 86.5% of the phosphopeptides still showed a >2-fold change in abundance, as well as clearly defined expression patterns (Figures S2B–S2D).

Overall, it is remarkable that ~76% of all detected proteins change at least 2-fold in relative abundance and/or phosphorylation state across the cellular contexts analyzed (Figure 2G). Proteins and phosphopeptides can be divided into similar expression pattern groups (color-coded in Figures 2B, 2C, 2E, and 2F). However, phosphopeptide expression appears to be much more tightly regulated and dynamic, as illustrated by the more nuanced patterns detected. These observations suggest that the sequential waves of protein phosphorylation rely on stage-specific deployment of kinases and/or phosphatases.

Sequential waves of kinase activity during meiosis

To systematically estimate kinase activities throughout gametogenesis, we used a curated collection of kinase-substrate pairs.[37] This allowed us to infer the activity status of 20 kinases for which multiple well-characterized substrates were detected in our dataset. Interestingly, most of the kinases analyzed showed a distinct and context-restricted pattern of activity, and, viewed as a whole, kinase activities peaked sequentially (Figure 2H; Table S3), resembling the consecutive waves of phosphopeptide expression described above (Figure 2F). Even though the deduced activity profile remains to be experimentally validated for most kinases, the inferred activity profile for $Cdc28^{CDK1}$, Chk1/Rad53, $Mec1/Tel1^{ATR/ATM}$, $Cdc5^{PLK1}$, and Ime2, among others, is supported by previous studies (Figure 2H).[30,39–41]

Complementary sequence analyses revealed enrichment of short-linear motifs in the vicinity of phosphorylation sites that are compatible with specific kinases being responsible for a significant proportion of the phosphorylation events in several of the phosphopeptide clusters (Figure S2E). For example, the preferred Ime2 motif (RPxS/T*)[42] was enriched in cluster P5, which fits well with the activity profile of Ime2 (Figure 2H); the activity profile of $Mec1/Tel1^{ATR/ATM}$ was consistent with the enrichment of (S/T*Q) in clusters P3 and P14 (compare Figures 2F and S2E); the activity profile of $Cdc28^{CDK1}$ matched the enrichment of (S/T*PxK/R) in clusters P6 and P2; the activity profile of $Cdc5^{PLK1}$ was consistent with the enrichment of (D/E/NxS/T*) in clusters P12 and P16. We noted that cluster P12 contains an additional enrichment for acidic and phospho-acceptor residues at positions −7, −4, and −3. Taking this motif[43] and the timing of phosphorylation into account (Figure 2F), we hypothesize that a subset of these phosphopeptides may be targeted by Casein Kinase $Hrr25^{CK1}$, which is phosphorylated at the onset of meiosis I (Figure S3B; Table S2) and is required for several aspects of chromosomes segregation and meiotic exit.[26,44]

Overall, the analyses above suggest that dynamic regulation of kinases and their likely interplay with phosphatases plays a major role in the establishment of the meiotic waves of protein phosphorylation. In combination with the patterns of phosphopeptide expression (Figure 2F) and GO heatmaps in the sections below (Figures 4A and 5A; Table S3), the kinase activity profiles and phosphorylation motif analyses should provide valuable insights as to which kinase(s) might be involved in the modification of specific proteins, complexes, or pathways of interest.

Meiosis-specific phosphorylation of proteins of unknown function

Next, we sought to estimate the robustness of the resource by analyzing the expression and phosphorylation of proteins of unknown function. We found that 91 proteins lacking annotated functions are phosphorylated in the cellular contexts analyzed, with the majority of phosphorylation events being upregulated in meiotic cells: 86% of the phosphopeptides in 60/91 proteins (Figures 3A–3C). To validate these data, we chose three candidates to be analyzed further based on their distinct phosphopeptide expression profiles: (1) Yer079w, phosphorylated in G0/G1 and throughout meiosis; (2) Ydl186w, phosphorylated at the onset of meiosis I; (3) Ymr196w, phosphorylated at late stages of meiosis (Figure 3D).

To monitor protein expression by western blotting, we tagged the genes with *myc9*. We were able to detect shifts in electrophoretic mobility that closely matched the pattern of phosphorylation determined by SWATH-MS (Figure 3E). Moreover, in all cases, the electrophoretic mobility shifts were sensitive to phosphatase treatment (Figure 3F). These data further confirm that a significant fraction of proteins of unknown function is phosphorylated in meiosis, and some of these might have important functions during gametogenesis. Given the defined set of candidate proteins/genes (Figure 3C), it is straightforward to envision genetic screens to explore both the function of each protein as well as the putative roles of phosphorylation.

Coordinated phosphorylation of dozens of cellular pathways

Having focused on proteins of unknown function, we next wanted to gain a comprehensive understanding of how phosphorylation impacts known cellular pathways during gametogenesis. To this end, we performed GO enrichment analyses across the time-resolved meiotic phosphoproteome. A wide range of cellular processes showed a pattern of enrichment in defined contexts (Figure 4A; see Figure S3A for the unenriched proteome; Table S3). For example, phosphorylation of factors associated with translation, cell polarity, and cytokinesis was high in mitotically dividing cells while being comparatively low in cells undergoing meiosis. Conversely, a vast range of biological processes peaked sequentially throughout gametogenesis. Among others, lipid transport, mRNA catabolic processes, and target of rapamycin (TOR) signaling peaked during pre-meiotic G0/G1, or shortly after induction of meiosis. DNA recombination, chromatin modification, and chromosome segregation peaked between prophase I and the meiotic divisions. Finally, processes such as lipid metabolism, mitophagy, and mitochondrial inheritance peaked at late stages of gametogenesis (Figure 4A).

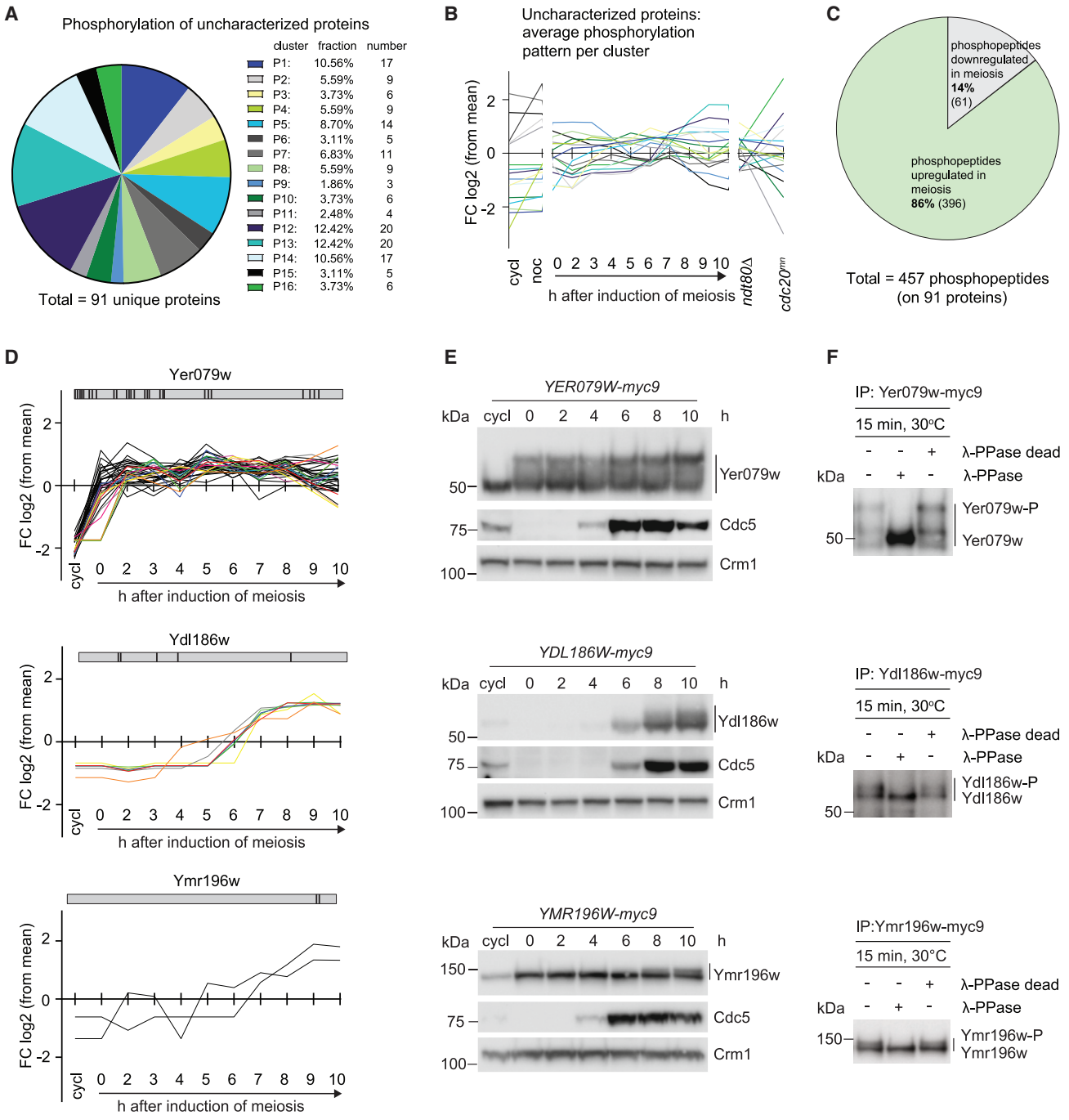

Figure 3. Meiotic phosphorylation of uncharacterized proteins during gametogenesis

(A) Pie chart depicting the distribution of phosphorylated proteins per cluster originating from uncharacterized open reading frames (ORFs), separated according to the clusters determined in Figure 2F. Note: phosphopeptides originating from the same protein can be part of different clusters, leading to multiple detections of unique proteins.

(B) Average SWATH-MS expression profiles of phosphopeptides originating from uncharacterized ORFs per cluster. Color-coded as in (A).

(C) Fraction of phosphopeptides originating from clusters that show upregulation in meiosis (green) and clusters that show downregulation in meiosis (gray).

(D) SWATH-MS expression profile of phosphopeptides of the uncharacterized proteins Yer079w, Ydl186w, and Ymr196w from Figure 2F (not corrected for protein abundance). Note: phosphopeptides that do not significantly change in abundance or that change in abundance but do not cluster are not shown.

(E) Western blot analysis of myc9-tagged proteins corresponding to (D). Proteins were detected using an anti-myc antibody. Cdc5 antibody was used as a cell-cycle stage marker. Crm1 serves as a loading control.

(F) Myc9-tagged proteins from (E) were immuno-affinity purified from prophase I cultures, in a *ndt80Δ* background (8 h in SPM). Proteins were treated with native or inactivated λ-phosphatase (λ-PPase), as indicated, and analyzed by western blotting.

See also Table S3.

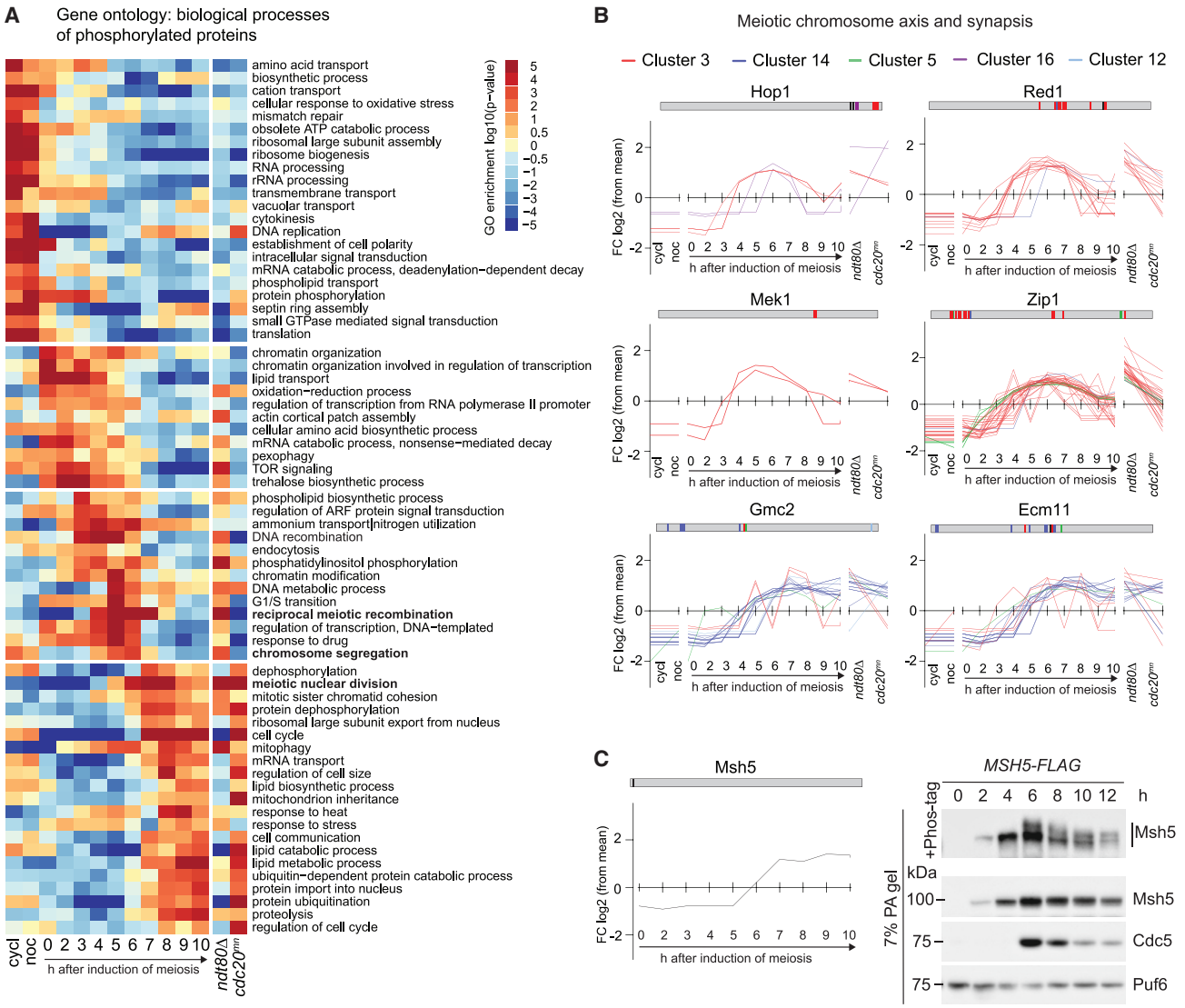

Figure 4. Sequential phosphorylation of cellular components with related biological functions

(A) Significant enrichment scores (abs(log10(*p* value)) ≥ 2) of Gene Ontology (GO) terms associated with biological processes in at least one condition from Figure 1A. The heatmap shows GO biological processes with increased (red) and decreased (blue) protein phosphorylation levels relative to the mean levels across all biological samples. For details, refer to STAR Methods. A complete list of GO terms including the scoring proteins can be found in Table S3.

(B) Dynamic changes in phosphopeptide expression of synaptonemal complex and chromosome axis-associated proteins. The plotted values represent the $\log_2$ fold change (FC) in each sample compared with the average phosphopeptide expression from all samples, as in Figure 2F (not corrected for protein abundance). The protein scheme above each graph indicates the position of the detected phosphorylation site(s). Phosphopeptides with similar expression patterns are plotted in the same color. See Tables S1 and S2 for the complete list of phosphopeptides. Note: phosphopeptides that do not significantly change in abundance or that change in abundance but do not cluster are not shown.

(C) Left: expression profile of a Msh5 phosphopeptide. Right: western blot analysis of Msh5-FLAG expression during meiosis at 2 h intervals after transfer to SPM. Puf6 serves as protein normalization control. A Phos-tag gel (top blot) was used to visualize the phospho-modification of Msh5-FLAG, which is otherwise not detectable in a 7% PA gel (bottom blots).

See also Figure S3 and Tables S1, S2, and S3.

These analyses suggest that various, possibly most, cellular processes are targeted by phosphorylation throughout gametogenesis. For many of these processes, there is a good correlation between the peak of phosphorylation and the expected timing of functional relevance (compare to Figures 1A and S1A–S1E). Therefore, it is likely that the regulated waves of protein phosphorylation play a pervasive role in orchestrating the unique order of cellular events that drive gametogenesis.

Dynamic phosphorylation of proteins controlling meiotic recombination and chromosome segregation

To further validate the phosphoproteomic census as a resource for hypothesis generation, we centered our analyses on

meiosis-specific pathways that are known to be regulated by kinases/phosphorylation. First, we focused on the mono-orientation of sister kinetochores, a process controlled by the cell-cycle kinases DDK and $Cdc5^{PLK1}$ and by five centromere-associated proteins: $Spo13^{Meikin}$ and the four monopolin complex subunits Mam1/Lrs4/Csm1/$Hrr25^{CK1}$. Mam1, Lrs4, and Spo13 were previously shown to be phosphorylated.[26,47,48] However, the modifications were inferred from electrophoretic mobility shifts or predicted based on consensus phosphorylation motifs, and it has remained unclear which residues become modified *in vivo*. Within our dataset, we found that multiple residues in Mam1, Lrs4, and Spo13 are modified during meiosis, with most sites peaking in expression during prophase I or metaphase I (Figure S3B, compare *ndt80Δ* vs. $cdc20^{mn}$). Interestingly, we also found that $Hrr25^{CK1}$ is phosphorylated at the onset of the first meiotic division.

Next, we focused on proteins involved in recombination, particularly on components of the SC, which controls multiple aspects of meiotic DNA repair.[49,50] SC assembly, maturation, and disassembly depend on several essential kinases,[41,51–54] but it remains poorly understood when the different SC components are modified and whether temporal/functional relationships exist in their modifications. We found numerous phosphorylation sites in all meiosis-specific SC components, including Hop1, Red1, Mek1, Zip1, Gmc2, and Ecm11. Interestingly, phosphorylation sites clustered in defined regions of each protein, suggesting that such regions might be particularly important for the regulation of protein function (Figure 4B). We also noticed that all six proteins were phosphorylated with similar patterns between pre-meiotic S-phase and metaphase I but with subsets of residues having slightly different phosphorylation kinetics (Figure 4B, note the five clusters).

In addition to monopolin and SC components, many other factors involved in chromosome segregation and meiotic DNA repair were phosphorylated during meiosis (Table S2). For example, we found that Msh5, a component of the MutSγ complex (Msh4-Msh5) that is crucial for the process of crossing over,[55] is modified at the prophase I-to-metaphase I transition (Figure 4C, left). This finding was confirmed using Phos-tag SDS-PAGE and western blotting (Figure 4C, right). Interestingly, recent work has established that phosphorylation of Msh4 throughout prophase I is required for the stability of MutSγ at recombination sites on chromosomes.[56] Since phosphorylation of Msh5 occurs later, coincident with exit from pachytene and loss of MutSγ from chromosomes (Figure 4C, right, note correlation with Cdc5 expression), it is possible that its modification plays a different/opposing role in the control of MutSγ function. Overall, these data facilitate the selection of sites for targeted mutagenesis to interrogate the mechanistic basis by which phosphorylation controls recombination and kinetochore function during meiosis. Since multiple SC and kinetochore components are modified with similar kinetics, future work should consider cooperativity and/or redundancy between phosphorylation events.

Coordinated phosphorylation events within protein complexes

The observation that multiple components of the monopolin and SC are phosphorylated in a stage-specific manner (Figures 4B and S3B) prompted us to systematically query if other protein complexes are modified in a concerted manner. To this end, we used a curated catalog of protein complexes[45] for which at least two subunits and six phosphopeptides were detected in our dataset. We then generated a heatmap combining the relative phosphorylation of each complex across all samples analyzed. We found that subunits of more than thirty protein complexes are coordinately phosphorylated in preparation for and throughout gametogenesis (Figure 5A; Table S3). Furthermore, akin to our previous observations in the GO enrichment analyses, the phosphorylation of most complexes was context-specific, and, in various instances, we noticed a correlation between the peak of phosphorylation and the expected timing of functional relevance (Figure 5A, e.g., SC, monopolin complex, the chromosomal passenger complex [Sli15/Bir1 complex]). These data raise the possibility that simultaneous phosphorylation of multiple subunits within a protein complex indicate functional significance. We set out to test this hypothesis by investigating the biological relevance of phosphorylation of the F_oF_1-ATP synthase complex, which undergoes transient modifications during early stages of meiosis (Figures 5B, 5C, S4A and S4B).

Phosphorylation of the mitochondrial F_oF_1-ATP synthase complex is required for efficient sporulation

We chose to focus on the F_oF_1-ATP synthase complex for three reasons: (1) despite its evolutionary conservation and extensive research on its structure and function, little is known regarding the regulation through phosphorylation.[57,58] (2) The core subunits of this complex are crucial for meiosis and for mitotic proliferation when a fermentable carbon source is absent, but they are not required for vegetative growth in medium containing glucose.[15,59] Therefore, it should be straightforward to assess the specificity of potential phenotypes in phosphorylation-resistant mutants. (3) As further discussed below, we have observed that numerous cellular processes related to mitochondrial function undergo dynamic modifications during meiosis. In this light, we have prioritized the study of processes associated with mitochondria.

We began by analyzing the sporulation efficiency of single F_oF_1-ATP synthase mutants carrying alanine substitutions in phosphorylated serines/threonines. Interestingly, all mutant strains showed a small but comparable reduction in sporulation efficiency (Figures 5E, 5G, and S4F–S4H). However, none of the mutations altered protein expression (Figures 5D, 5F, and S4C–S4E), nor did they affect vegetative growth in medium containing glycerol or glucose (Figures S4I–S4L). Moreover, we noticed that $atp2^{S25A}$ $atp7^{S109A}$ double mutants showed no additive reduction in sporulation efficiency (Figure S4H), suggesting that the loss of function is unlikely to be a consequence of structural disruptions caused by the alanine substitutions. Overall, these data indicate that F_oF_1-ATP synthase phosphorylation plays a role during meiosis. Given the similar kinetics of phosphorylation and the comparable reduction in sporulation efficiency in all phosphorylation-resistant mutants tested (single and double mutants), we envision that phosphorylation of different subunits may be part of the same mechanism that modulates F_oF_1-ATP synthase function to match the specialized needs of gametogenesis.

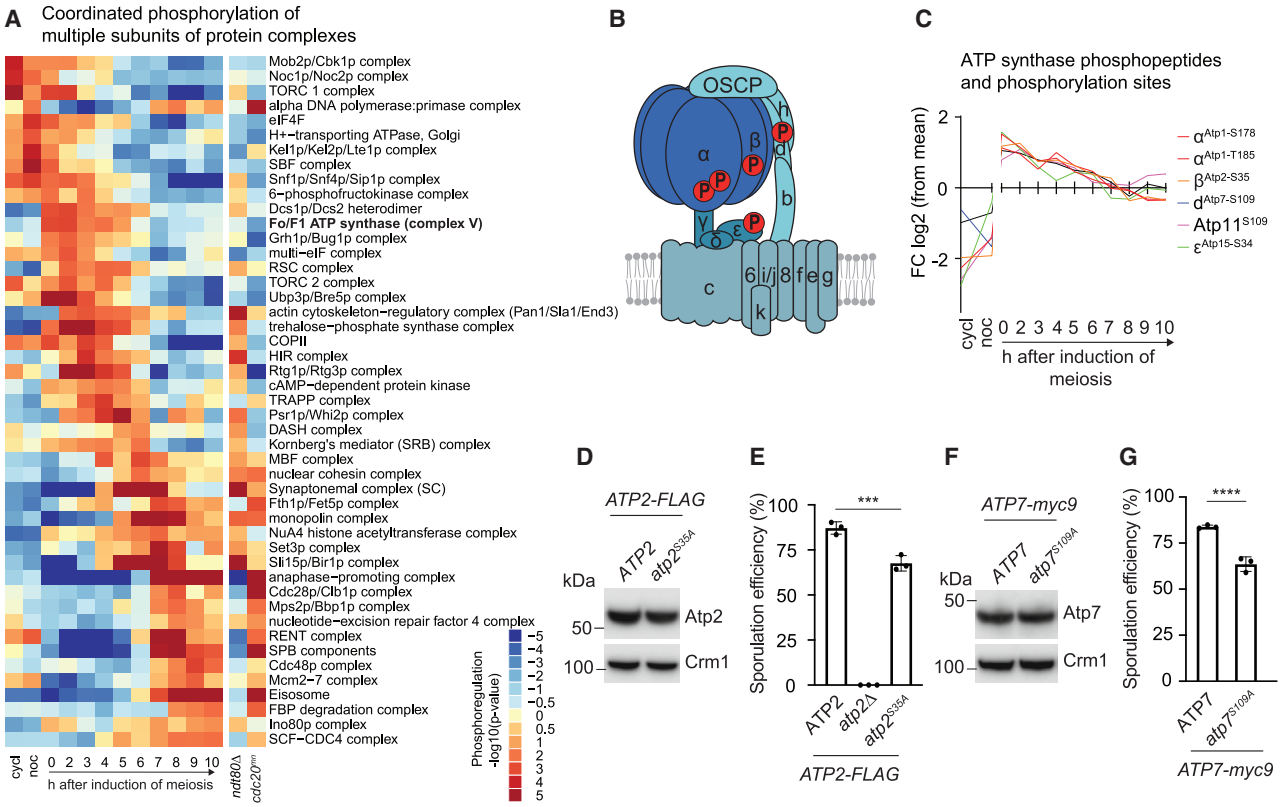

Figure 5. Coordinated phosphorylation of multiple protein complex subunits: F_oF_1-ATP synthase phosphorylation is required for efficient gametogenesis.

(A) Heatmap with known protein complexes[45] in which multiple subunits are coordinately phosphorylated. Cutoff applied was (abs($\log_{10}$(*p* value)) ≥ 1) compared with the mean phosphorylation in at least three samples. Protein complexes were included if at least two of its subunits were phosphorylated and at least six individual phospho-sites in a complex were reported. Red indicates concertedly upregulated phosphorylation when compared with the average phosphorylation levels across all samples analyzed; blue indicates downregulation. FC > 5 or < −5 are capped. See Table S3 for the complete list of proteins.

(B) Schematic model of a monomer of the mitochondrial F_oF_1-ATP synthase complex, adapted from Song et al.[46] Proteins found to be phosphorylated are indicated.

(C) Dynamic changes in phosphopeptide expression of F_oF_1-ATP synthase subunits, extracted from Figure 2F. The legend on the right contains the systematic name of each subunit and phosphorylated residue in each of the phosphopeptides plotted. See Table S2 for the detailed list of phosphopeptides.

(D) Asynchronous mitotic cultures of cells expressing *ATP2-FLAG* or *atp2^{S35A}-FLAG* from the endogenous locus were analyzed by western blotting for the indicated proteins. Crm1 serves as loading control.

(E) Cells with the indicated genotypes were sporulated for 24 h. Sporulation efficiency was assessed by monitoring the morphology of 200 cells per condition. Plotted values indicate mean ± SD from three replicates (two-tailed, unpaired t test, ***$p < 0.001$, ****$p < 0.0001$).

(F) As in (D) for cells expressing *ATP7-myc9* or *atp7^{S109A}-myc9*, as indicated.

(G) As in (E) for cells expressing *ATP7-myc9* or *atp7^{S109A}-myc9*, as indicated.

See also Figure S4 and Tables S2 and S3.

Ultrastructural changes in mitochondrial organization visualized by cryoET

In addition to F_oF_1-ATP synthase phosphorylation, we noticed that various biological processes associated with mitochondria were upregulated during gametogenesis (Figure 6A). For example, proteins involved in mitochondrial genome maintenance, ATP synthesis, and mitochondrial protein translation peaked at the onset of meiosis. Aerobic respiration, oxidative phosphorylation, and the tricarboxylic acid (TCA) cycle were more pronounced later on, while the phosphorylation of proteins linked to mitochondrial dynamics and mitochondrial inheritance was upregulated toward the end of meiosis. These broad and dynamic alterations led us to postulate that mitochondria have specialized features during meiosis, which might be captured using orthogonal approaches. Therefore, prompted by the proteomics data, we set out to study the ultrastructure of meiotic mitochondria using cryoET, an imaging approach that enables the visualization of mesoscale assemblies in a near-native state, *in situ*.[61] To do so, we plunge-froze yeast cells during vegetative growth, pre-meiotic G0/G1, meiotic prophase I, as well as spores. We then thinned frozen-hydrated cells using cryofocused ion beam (FIB) milling and visualized the prepared lamellae by cryoET.[62]

We observed two notable changes in the mitochondrial ultrastructure across the cellular contexts analyzed. First, as cells progressed through gametogenesis, we measured a decrease in mitochondrial area in cross-sections of tomograms, reaching the lowest value in spores (Figures 6B, 6C, and S5A). The

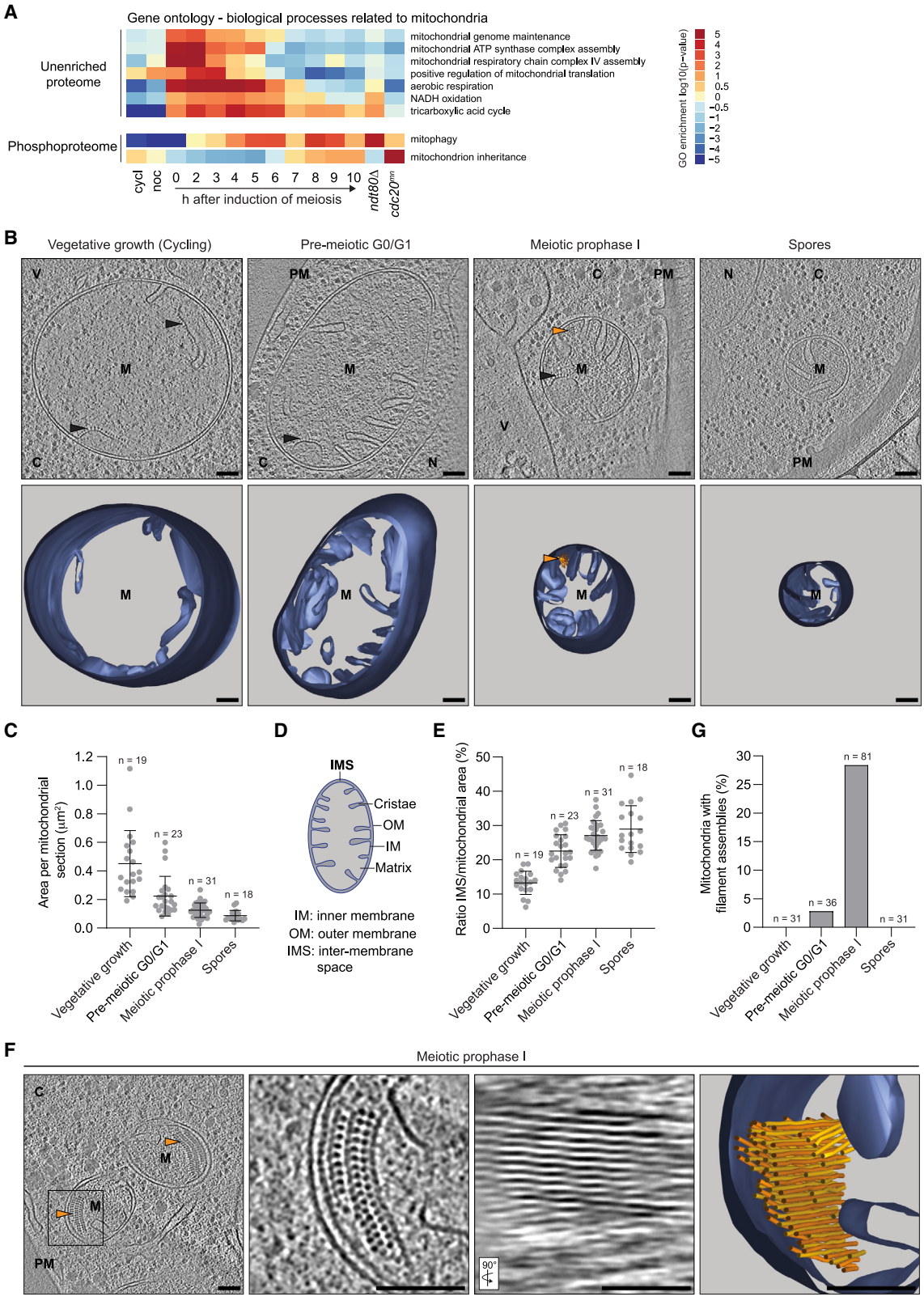

(legend on next page)

decreased area could indicate that the mitochondria become smaller and/or more tubular, as proposed previously[63] (Figure S5A). Second, we noted an increase in the ratio of the inter-membrane space to mitochondrial area, which reached the highest value in spores (Figures 6D and 6E). This relative increase in inter-membrane space is consistent with the high metabolic requirements and with the essential function of mitochondria in meiotic cells. The changes in overall morphology might be functionally linked to the many changes in the expression and/or phosphorylation of mitochondrial-associated proteins detected by mass spectrometry (Figures 6A, S5B, and S5C).

Transient formation of mitochondrial Ald4^{ALDH2} filaments during gametogenesis

While closely inspecting the ultrastructure of mitochondria throughout meiosis, we observed a significant fraction of tomograms containing ordered arrays of densities (Figures 6B and 6F, orange arrowheads). Side views of the cryo-tomograms revealed that these arrays consist of straight filamentous assemblies that associate laterally into bundles (Figure 6F; see segmentation model). These filamentous assemblies were sporadically present in mitochondria from pre-meiotic G0/G1 cells but were absent during vegetative growth and could not be detected in the mitochondria inherited by mature spores (Figure 6G). This intriguing observation motivated us to develop methodology to characterize filament composition. In an accompanying study,[60] we have established a cryoEM/ET workflow, termed FilamentID, that allowed us to obtain a structure of the filaments at sub-4 Å resolution. Using the proteomics data in Figure 2, we then generated a short list of mitochondrial proteins[64] whose abundance increases during meiosis. By docking AlphaFold[65,66] structural predictions of the mitochondrial candidates into the filament structure, we found the mitochondrial filaments to be composed of the conserved aldehyde dehydrogenase Ald4^{ALDH2} (see accompanying study by Hugener et al.[60]) (Figures 7A and 7B). Based on previous work showing that aldehyde dehydrogenases form tetramers,[67] it is likely that Ald4^{ALDH2} filaments assemble from the stacking of tetramers, which act as the building blocks for polymerization (Figure 7A).

Phosphorylation-resistant Ald4 mutants are defective in filament formation

Having the phosphoproteomics dataset at hand prompted us to query whether Ald4 was phosphorylated, representing a possible mechanism to enable regulated polymerization. We found that at least three serines are modified throughout meiosis: S96, S269, and S500 (Figures 7C and 7D). To test if phosphorylation influences Ald4 filament assembly, we generated a mutant strain encoding alanine substitutions replacing the phosphorylated serines (*ald4^{3A}*), and to monitor the presence of mitochondrial filaments in purified mitochondria by cryoET. Whereas ~25% of meiotic mitochondria from *ALD4^{WT}* control cells contained Ald4 filaments, we were unable to observe these filaments in mitochondria from *ald4^{3A}* mutants (Figures 7E and 7F). To determine if the alanine substitutions impacted protein levels or the subcellular localization of Ald4^{3A}, we raised an antibody against Ald4. This was necessary because the presence of a tag interfered with the ability of Ald4 to polymerize (Figures 7A and S6A). Western blot and *in situ* immunofluorescence analyses showed that the Ald4^{3A} mutant protein accumulated and localized to mitochondria efficiently (Figures S6B and S6C), indicating that the mutations neither impair protein stability nor mitochondrial localization. By analyzing the electrophoretic mobility in native PAGE conditions, we also observed that the majority of Ald4^{WT} and Ald4^{3A}—that entered the gel—migrated between protein markers with 242 and 480 kDa (Figure S6D). This would be consistent with Ald4^{3A} being able to self-associate and form tetramers (predicted 226.7 kDa) or dimers of tetramers (predicted 453.4 kDa). Interestingly, we did notice that a fraction of Ald4^{3A} displayed a lower electrophoretic mobility (Figure S6D, smear above the main bands). These species could represent polymerization intermediates that fail to assemble into long polymers, with long polymers possibly failing to enter the gel due to the very large size of 200–500 nm and a molecular weight of several thousand kilodalton (Figure 6F). In agreement with this notion, we also found that Ald4-GFP fusions, which would be expected to be defective in polymerization due to the presence of the bulky tag on the C-terminus (Figure S6A), accumulated in a broad range of high molecular weight complexes with reduced

Figure 6. Mitochondrial ultrastructure during meiosis

(A) Extracts from GO analyses in Figures 4A and S3A showing mitochondria-associated processes.

(B) Visualization of mitochondria using cryo-electron tomography (cryoET). Top: slices through cryo-tomograms of FIB-milled budding yeast cells with examples of mitochondria from the stages indicated; prophase I (8 h in SPM, *ndt80Δ*); and spores (24 h in SPM). Shown are projections of 9.14 nm (cycling and spores) and 8.68 nm (pre-meiotic G0/G1 and meiotic prophase I) thick slices. Bottom: corresponding segmentation models of cryo-tomograms. M, mitochondrion; C, cytoplasm; V, vacuole; PM, plasma membrane; N, nucleus. Scale bars, 100 nm. Rows of F_oF_1-ATP synthase (black arrowheads) and filament arrays (orange arrowhead) are highlighted.

(C) Area of mitochondrial sections from cryo-tomograms in (B). The number of mitochondria imaged per condition is indicated (n) and represents cumulated results from one to seven independent cell cultures per condition. Mean value ± SD is displayed.

(D) Schematic of mitochondrial membrane architecture. Shown are cristae, the matrix, the inner membrane (IM), the outer membrane (OM), and the inter-membrane space (IMS).

(E) The IMS/mitochondrial area ratio was determined from the mitochondria analyzed in (C). Mean value ± SD is displayed.

(F) Filament arrays within meiotic prophase I mitochondria (*ndt80Δ*, 8 h in SPM). Left: example cryo-tomogram of a FIB-milled cell with filament arrays (orange arrows) inside mitochondria. Middle: enlarged views (different y-axis rotation compared with the overview) of one filamentous array together with the corresponding side view. Shown are projections of 9.14 nm and 18.28 nm (enlarged views) thick slices. Right: segmentation model highlighting mitochondrial membranes (blue) and filaments in (orange and yellow). Note the regular arrangement of single filaments within the assembly. M, mitochondrion; C, cytoplasm; PM, plasma membrane. Scale bars, 100 nm.

(G) Proportion (%) of mitochondria containing filament assemblies as described in (F). The number of mitochondria inspected for filamentous assemblies is indicated (n) and represents cumulated results from one to seven independent cell cultures per condition. Note: a subset of the data is also shown in Hugener et al.[60]

See also Figure S5 and Table S3.

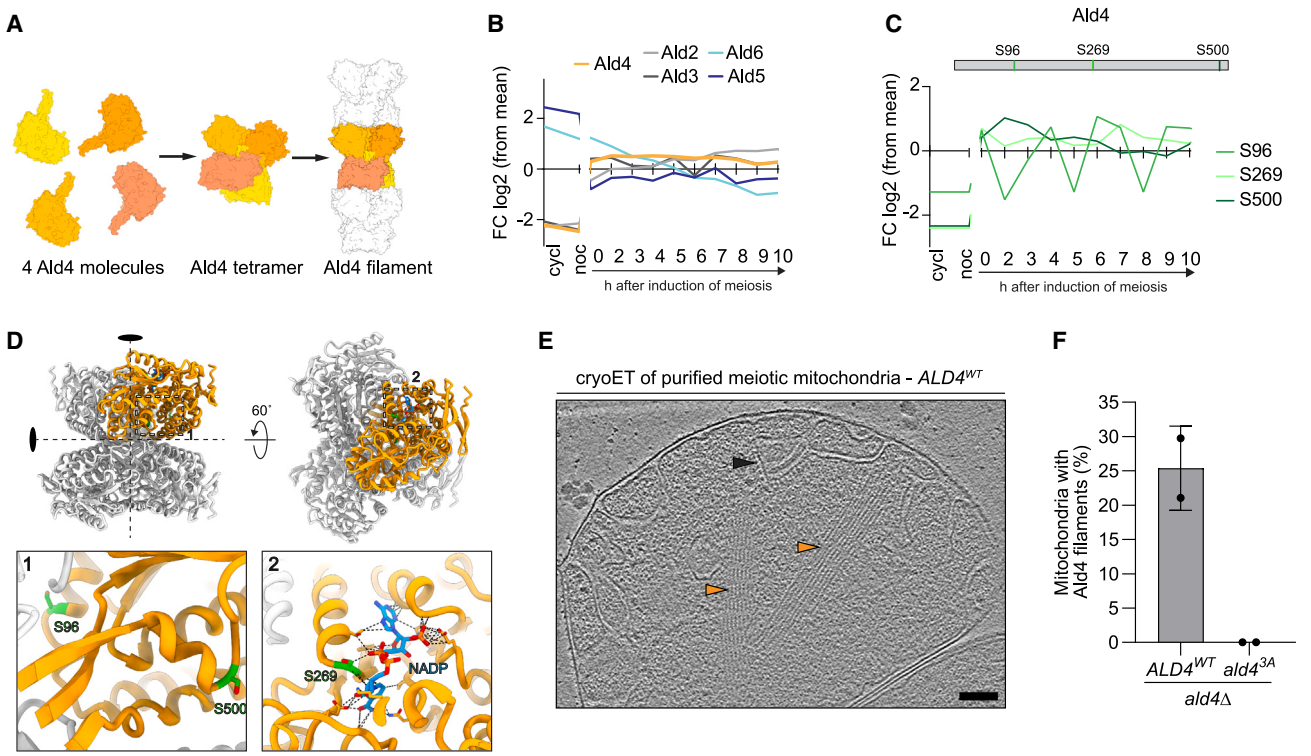

Figure 7. Phosphorylation might regulate the accumulation of Ald4 filaments

(A) Schematic representation of Ald4 monomers forming a tetramer. Individual Ald4 tetramers can further assemble into filaments.

(B) Dynamic changes in protein expression for Ald2, Ald3, Ald4, Ald5, and Ald6, extracted from Figure 2C. The plotted values represent the $\log_2$ fold change (FC) in each sample compared with the average protein expression from all samples.

(C) Ald4 phosphopeptide expression. The plotted values represent the $\log_2$ FC in each sample compared with the average phosphopeptide expression from all samples, as in Figure 2F. The protein scheme above the graph indicates the position of the detected phosphorylation sites.

(D) Ribbon and stick diagram showing the meiotic phosphorylation sites on the Ald4 tetramer (PDB: 8RWK).[60] One Ald4 monomer is colored orange, while the other subunits are colored white. The ellipses indicate the positions of the 2-fold symmetry axes. The phosphorylation sites (S96, S269, and S500) are colored green and are highlighted with enlarged views at the bottom, where side chains and the co-factor NADP are labeled and are shown in stick style.

(E) Slice through a cryo-tomogram of a purified mitochondrion containing Ald4 filament arrays (orange arrowheads) and rows of F_oF_1-ATP synthases (black arrowhead). Cells were collected 6 h after induction of meiosis in SPM medium. Shown are projections of 5.35 nm thick slices. Scale bars, 100 nm.

(F) Purified mitochondria from phosphorylation-resistant Ald4 mutants undergoing meiosis (6 h in SPM) were imaged by cryoET as in (E). The mean percentage of mitochondria containing filaments for each genotype is shown for two independent experiments. ≥33 mitochondria were analyzed per genotype in each of the two experiments. Mean ± SD is displayed.

See also Figure S6.

electrophoretic mobility (Figures S6E and S6F). These species are likely to reflect polymerization intermediates or aberrant aggregates (Figure S6A).

Finally, we attempted to investigate the cellular function of Ald4 polymers. In mouse models, the mitochondrial homolog of Ald4, ALDH2, was shown to mediate aldehyde detoxification to maintain genome stability in the germline.[68] Since Ald4 was strongly expressed (Figure 7B, orange line) and formed ordered filament arrays during meiosis, we hypothesized that it may play an important role during yeast gametogenesis. However, we found that *ald4Δ* mutants sporulated efficiently, and *ald4Δ* spores retained the full ability to germinate (Figures S6G and S6H). In addition to Ald4, yeast cells contain four additional aldehyde dehydrogenases (Ald2, Ald3, Ald5, and Ald6), all of which were robustly detected in our proteomics dataset, with Ald2 and Ald3 being strongly induced during meiosis (Figure 7B, gray lines). Therefore, we considered that functional redundancy might explain the lack of an obvious phenotype in *ald4Δ* mutants. However, *ald2-6Δ* quintuple mutants showed normal levels of spore viability and only a mild reduction in sporulation efficiency (Figures S6G and S6H). Hence, we conclude that Ald4, and more broadly the combined function of Ald enzymes, is largely dispensable for sporulation and spore viability in the laboratory conditions tested.

Overall, the data above show that Ald4 is phosphorylated during meiosis and that phosphorylation-resistant mutants are unable to accumulate large filaments that can be visualized by cryoET. Since $Ald4^{3A}$ remains capable of localizing to mitochondria and to form high molecular weight species that are compatible with the assembly of tetramers, we propose that phosphorylation may be involved in the regulation of tetramer stacking to generate long Ald4 filaments. Future work will be required to dissect further the mechanistic basis by which phosphorylation regulates polymer formation as well as to systematically probe for Ald4 function in conditions that mimic the environmental challenges that meiotic cells experience in the wild. The identification

of such conditions will then enable the study of the biological relevance of Ald4 filament formation using the *ald4*^{3A} allele.

DISCUSSION

Gametes are specialized cells that carry a unique assortment of an organism's genetic information from one generation to the next.[1] To understand how gametes form, we employed a comprehensive systems-level approach to monitor the proteome throughout the entire differentiation program, from pre-meiotic G0/G1 to spore formation. We found that protein phosphorylation targets components of virtually all cellular pathways. Interestingly, most phosphorylation events occurred in a regulated and stage-specific manner (86% of phosphopeptides). Moreover, multiple components of the same cellular pathway, or even different subunits of the same protein complex, were frequently found to be coordinately modified. Considering that PTMs are commonly employed to diversify and control protein function,[69,70] it is likely that the waves of phosphorylation observed during meiosis play a substantial role in rewiring the proteome to meet the specialized cellular requirements of gamete formation. Importantly, more than 1,700 of the approximately 9,400 dynamically tracked phosphorylation sites were not reported in Lanz et al.[28] or the BioGRID repository,[36] and only a small portion of them are found on meiosis-specific proteins. This suggests that beyond occurring in global, sequential waves, phosphorylation fine-tunes the proteome to enable efficient gametogenesis. In this context, our finding that phosphorylation of the mitochondrial F_oF_1-ATP synthase is required for efficient sporulation already provides a striking example of how context-specific modification of a ubiquitous enzyme plays unexpected roles in regulating gametogenesis.

In the following sections, we share our perspective on how the meiotic census can serve as a resource for hypothesis generation. Additionally, we discuss how we have already leveraged this resource in combination with *in situ* cryoET imaging to gain further insights into the dynamic behavior of meiotic mitochondria.

The meiotic protein expression and phosphorylation census as a resource for hypothesis generation

Protein kinases and phosphatases are known to exert control over multiple biological processes, including meiosis.[20,23,71] It remains a significant challenge, however, to identify the direct target(s) of each kinase, which is a critical step for gaining a deeper understanding of both kinase and substrate function. Conversely, individual components of many cellular pathways have been inferred to undergo regulated phosphorylation during meiosis. Nevertheless, we often lack the precise location of the modified residue(s) and the responsible kinase. Our dataset does not establish direct kinase-substrate relationships, but it holds significant value for generating testable hypotheses. On one hand, it presents robust evidence for phosphorylation occurring in a diverse set of proteins with essential meiotic functions, as well as in proteins without any annotated functions. On the other hand, the heatmaps of kinase activity (Figure 2H) supported by phosphorylation motif analysis (Figure S2E) can be readily correlated with the patterns of phosphorylation of individual proteins (Figure 2F), protein complexes (Figure 5A), and biological processes (Figure 4A). Using this approach, we have recently harnessed this resource to identify the direct targets of Polo-like kinase Cdc5^{PLK1} in the regulation of nuclear pore complex disassembly during meiosis I.[21]

The observation that multiple components within protein complexes/biological pathways are frequently phosphorylated in a concerted manner can also be indicative of functional relevance and, as such, helpful for hypothesis generation. Based on our findings with the F_oF_1-ATP synthase, we envision that this resource will serve as the starting point for the systematic study of the roles of phosphorylation in a variety of biological processes that are of relevance for gametogenesis. We also expect that the careful analysis of this dataset will uncover intriguing and unforeseen connections among processes and events that initially appear unrelated.

A final strength of this resource is that the data recording and analysis in SWATH-MS is not restricted to pre-selected acquisition windows or peptide precursors.[32] Therefore, we obtained a near-complete picture of proteins and phosphoproteins that can be repeatedly queried to answer diverse biological questions when new information becomes available.

Combined proteomics and cryoET reveal specialized features of meiotic mitochondria

Encouraged by the prominent enrichment of mitochondria-associated processes that were captured by GO analyses (Figure 6A), we posited that *in situ* cryoET imaging may unveil structural changes in mitochondria that are linked to the proteomic changes. Consistent with this hypothesis and with the work of others,[3,63,72,73] we have observed striking alterations in mitochondrial morphology. Unexpectedly, we also observed that mitochondria from cells in prophase I contained arrays of filamentous assemblies (Figures 6F and 6G). Motivated by this observation, we have developed a multimodal imaging method in an accompanying study[60] to help identify the filament building block as the conserved aldehyde dehydrogenase Ald4^{ALDH2}.

The identification of cellular phenotypes associated with the loss of Ald4 will be of major relevance for studying the biological role(s) of Ald4 phosphorylation and filament formation. In addition to regulatory roles (e.g., enzymatic activation, inhibition, enzyme storage, etc.), we can envision scenarios in which Ald4 polymerization has functions that go beyond the canonical roles of aldehyde dehydrogenases. For example, filament formation could be used to sense and signal the metabolic state of individual mitochondria. We find that filamentous Ald4 is bound to its co-factor NADP(H) (Figure 7D).[60] Moreover, serine 269 contacts NADP(H) (Figure 7D, inset 2), and its phosphorylation could stabilize the binding of the co-factor. In turn, the NADP(H) binding pocket is located close to the surface that potentially mediate polymer formation (Figure 7D). Hence, there might be functional links between phosphorylation, NADP(H) binding, and polymer formation. In support of this notion, previous work using *ALD4* mutants that fail to be imported into mitochondria has suggested that both nucleotide binding and the enzyme active site are required for the accumulation of cytoplasmic rod-like Ald4 structures upon prolonged starvation.[74] This observation, however, has to be interpreted with caution since it is unclear whether such cytoplasmic assemblies represent the Ald4 filaments that we report here to form in meiotic mitochondria. Moreover, Ald4

was visualized using a GFP tag on the C-terminus, which our work (Figures S6A, S6E, and S6F), as well as previous work,[75] suggest to already interfere with the ability of Ald4 to form higher-order structures.

Our findings with Ald4 raise thought-provoking questions that would be interesting to follow up in other cellular contexts and biological systems. For example, the human mitochondrial homolog of Ald4, ALDH2,[76] plays a fundamental role in alcohol metabolism. The E487K polymorphism, residing in the oligomerization domain, results in the ALDH2*2 variant, which is present in approximately 8% of the world population and is responsible for the acute Asian flush syndrome.[77,78] This raises the question of whether ALDH2 can also form polymers and whether the inability to polymerize is linked to mitochondrial dysfunction and disease.

Limitations of the study

A limitation to consider is that SWATH-MS has inherent detection limits. Therefore, targeted analyses may be required to uncover the detailed expression pattern and/or the full extent of phosphorylation of some proteins. Because protein function is frequently regulated by PTMs, due to the scale, it will be challenging to ascertain the biological significance of all the numerous phosphorylation events documented here. Therefore, we anticipate that previously described prioritization strategies based on the integration of evolutionary conservation and structural information will be valuable in refining hypothesis building.[28,79–82]

STAR★METHODS

Detailed methods are provided in the online version of this paper and include the following:

- KEY RESOURCES TABLE
- RESOURCE AVAILABILITY
  - Lead contact
  - Materials availability
  - Data and code availability
- EXPERIMENTAL MODEL AND STUDY PARTICIPANT DETAILS
  - Saccharomyces cerevisiae
- METHOD DETAILS
  - Strain generation
  - Meiotic time courses and cycling cultures
  - FACS analysis of DNA content
  - Sporulation efficiency assay
  - Spore viability assay
  - Yeast spot assay
  - Immunofluorescence imaging
  - Protein analyses
  - MS data acquisition and analysis
  - Mitochondria isolation
  - Plunge-freezing
  - CryoFIB milling
  - CryoET data collection and processing
  - Mitochondrial ultrastructure analysis
- QUANTIFICATION AND STATISTICAL ANALYSIS

SUPPLEMENTAL INFORMATION

Supplemental information can be found online at https://doi.org/10.1016/j.devcel.2024.05.025.

ACKNOWLEDGMENTS

We thank Marco Hein for comments on the manuscript. ScopeM at ETH Zürich provided instrument access and support for cryo-ET imaging. The Max Perutz Labs BioOptics Light Microscopy facility provided support for the light microscopy experiments. The Beltrao lab is supported by the Helmut Horten Stiftung and the ETH Zurich Foundation. The Pilhofer Lab was supported by the NOMIS Foundation. The Matos Lab was supported by the Swiss National Science Foundation (SNSF) (155823 and 176108), the Austrian Science Foundation FWF (SFB Meiosis—8807-B), and the European Research Council (101002629).

AUTHOR CONTRIBUTIONS

R.W. performed meiotic time courses for MS experiments with help from M.A.; R.W. and L.G. processed samples for MS; L.G. performed the MS experiments, MS data processing, and initial data analysis; R.W. performed follow-up data analyses; Y.H.-A. performed protein complex, GO, and kinase activity analyses; R.W. performed sporulation efficiency, viability, and spot assays; J.H. performed cryoET experiments and data analysis, with help from F.W.; J.X. generated the structural model of Ald4 filaments; A.H. performed *in situ* IF experiments; J.v.G. performed kinase phosphorylation motif analyses; J.M., M.P., P.B., and R.A. conceived the study and acquired funding; R.W. and J.M. wrote the initial draft of the manuscript with contributions from M.P., J.H., and P.B.; all authors contributed to the final manuscript.

DECLARATION OF INTERESTS

The authors declare no competing interests.

Received: September 24, 2023
Revised: February 25, 2024
Accepted: May 20, 2024
Published: June 20, 2024

REFERENCES

1. Petronczki, M., Siomos, M.F., and Nasmyth, K. (2003). Un menage a quatre: the molecular biology of chromosome segregation in meiosis. Cell *112*, 423–440. https://doi.org/10.1016/s0092-8674(03)00083-7.
2. Marston, A.L., and Amon, A. (2004). Meiosis: cell-cycle controls shuffle and deal. Nat. Rev. Mol. Cell Biol. *5*, 983–997. https://doi.org/10.1038/nrm1526.
3. Suda, Y., Nakanishi, H., Mathieson, E.M., and Neiman, A.M. (2007). Alternative modes of organellar segregation during sporulation in Saccharomyces cerevisiae. Eukaryot. Cell *6*, 2009–2017. https://doi.org/10.1128/EC.00238-07.
4. Walther, T., Létisse, F., Peyriga, L., Alkim, C., Liu, Y., Lardenois, A., Martin-Yken, H., Portais, J.C., Primig, M., and François, J.M. (2014). Developmental stage-dependent metabolic regulation during meiotic differentiation in budding yeast. BMC Biol. *12*, 60. https://doi.org/10.1186/s12915-014-0060-x.
5. Bearer, E.L., and Friend, D.S. (1990). Morphology of mammalian sperm membranes during differentiation, maturation, and capacitation. J. Electron Microsc. Tech. *16*, 281–297. https://doi.org/10.1002/jemt.1060160403.
6. Schmerler, S., and Wessel, G.M. (2011). Polar bodies–more a lack of understanding than a lack of respect. Mol. Reprod. Dev. *78*, 3–8. https://doi.org/10.1002/mrd.21266.
7. Neiman, A.M. (2011). Sporulation in the budding yeast Saccharomyces cerevisiae. Genetics *189*, 737–765. https://doi.org/10.1534/genetics.111.127126.
8. Lennon, J.T., and Jones, S.E. (2011). Microbial seed banks: the ecological and evolutionary implications of dormancy. Nat. Rev. Microbiol. *9*, 119–130. https://doi.org/10.1038/nrmicro2504.

9. Rittershaus, E.S.C., Baek, S.H., and Sassetti, C.M. (2013). The normalcy of dormancy: common themes in microbial quiescence. Cell Host Microbe *13*, 643–651. https://doi.org/10.1016/j.chom.2013.05.012.

10. Sing, T.L., Brar, G.A., and Ünal, E. (2022). Gametogenesis: exploring an endogenous rejuvenation program to understand cellular aging and quality control. Annu. Rev. Genet. *56*, 89–112. https://doi.org/10.1146/annurev-genet-080320-025104.

11. Goodman, J.S., King, G.A., and Ünal, E. (2020). Cellular quality control during gametogenesis. Exp. Cell Res. *396*, 112247. https://doi.org/10.1016/j.yexcr.2020.112247.

12. Winter, E. (2012). The Sum1/Ndt80 transcriptional switch and commitment to meiosis in Saccharomyces cerevisiae. Microbiol. Mol. Biol. Rev. *76*, 1–15. https://doi.org/10.1128/MMBR.05010-11.

13. Sou, I.F., Pryce, R.M., Tee, W.W., and McClurg, U.L. (2021). Meiosis initiation: a story of two sexes in all creatures great and small. Biochem. J. *478*, 3791–3805. https://doi.org/10.1042/BCJ20210412.

14. Jambhekar, A., and Amon, A. (2008). Control of meiosis by respiration. Curr. Biol. *18*, 969–975. https://doi.org/10.1016/j.cub.2008.05.047.

15. Zhao, H., Wang, Q., Liu, C., Shang, Y., Wen, F., Wang, F., Liu, W., Xiao, W., and Li, W. (2018). A role for the respiratory chain in regulating meiosis initiation in Saccharomyces cerevisiae. Genetics *208*, 1181–1194. https://doi.org/10.1534/genetics.118.300689.

16. Mitchell, A.P. (1994). Control of meiotic gene expression in Saccharomyces cerevisiae. Microbiol. Rev. *58*, 56–70. https://doi.org/10.1128/mr.58.1.56-70.1994.

17. Chu, S., DeRisi, J., Eisen, M., Mulholland, J., Botstein, D., Brown, P.O., and Herskowitz, I. (1998). The transcriptional program of sporulation in budding yeast. Science *282*, 699–705. https://doi.org/10.1126/science.282.5389.699.

18. Cheng, Z., Otto, G.M., Powers, E.N., Keskin, A., Mertins, P., Carr, S.A., Jovanovic, M., and Brar, G.A. (2018). Pervasive, coordinated protein-level changes driven by transcript isoform switching during meiosis. Cell *172*, 910–923.e16. https://doi.org/10.1016/j.cell.2018.01.035.

19. Brar, G.A., Yassour, M., Friedman, N., Regev, A., Ingolia, N.T., and Weissman, J.S. (2012). High-resolution view of the yeast meiotic program revealed by ribosome profiling. Science *335*, 552–557. https://doi.org/10.1126/science.1215110.

20. Kar, F.M., and Hochwagen, A. (2021). Phospho-regulation of meiotic prophase. Front. Cell Dev. Biol. *9*, 667073. https://doi.org/10.3389/fcell.2021.667073.

21. King, G.A., Wettstein, R., Varberg, J.M., Chetlapalli, K., Walsh, M.E., Gillet, L.C.J., Hernández-Armenta, C., Beltrao, P., Aebersold, R., Jaspersen, S.L., et al. (2023). Meiotic nuclear pore complex remodeling provides key insights into nuclear basket organization. J. Cell Biol. *222*, e202204039. https://doi.org/10.1083/jcb.202204039.

22. Bhagwat, N.R., Owens, S.N., Ito, M., Boinapalli, J.V., Poa, P., Ditzel, A., Kopparapu, S., Mahalawat, M., Davies, O.R., Collins, S.R., et al. (2021). SUMO is a pervasive regulator of meiosis. eLife *10*, e57720. https://doi.org/10.7554/eLife.57720.

23. Swartz, S.Z., Nguyen, H.T., McEwan, B.C., Adamo, M.E., Cheeseman, I.M., and Kettenbach, A.N. (2021). Selective dephosphorylation by PP2A-B55 directs the meiosis I-meiosis II transition in oocytes. eLife *10*, e70588. https://doi.org/10.7554/eLife.70588.

24. Celebic, D., Polat, I., Legros, V., Chevreux, G., Wassmann, K., and Touati, S.A. (2024). Qualitative rather than quantitative phosphoregulation shapes the end of meiosis I in budding yeast. EMBO J. *43*, 1325–1350. https://doi.org/10.1038/s44318-024-00032-5.

25. Koch, L.B., Spanos, C., Kelly, V., Ly, T., and Marston, A.L. (2024). Rewiring of the phosphoproteome executes two meiotic divisions in budding yeast. EMBO J. *43*, 1351–1383. https://doi.org/10.1038/s44318-024-00059-8.

26. Petronczki, M., Matos, J., Mori, S., Gregan, J., Bogdanova, A., Schwickart, M., Mechtler, K., Shirahige, K., Zachariae, W., and Nasmyth, K. (2006). Monopolar attachment of sister kinetochores at meiosis I requires casein kinase 1. Cell *126*, 1049–1064. https://doi.org/10.1016/j.cell.2006.07.029.

27. Oelschlaegel, T., Schwickart, M., Matos, J., Bogdanova, A., Camasses, A., Havlis, J., Shevchenko, A., and Zachariae, W. (2005). The yeast APC/C subunit Mnd2 prevents premature sister chromatid separation triggered by the meiosis-specific APC/C-Ama1. Cell *120*, 773–788. https://doi.org/10.1016/j.cell.2005.01.032.

28. Lanz, M.C., Yugandhar, K., Gupta, S., Sanford, E.J., Faça, V.M., Vega, S., Joiner, A.M.N., Fromme, J.C., Yu, H., and Smolka, M.B. (2021). In-depth and 3-dimensional exploration of the budding yeast phosphoproteome. EMBO Rep. *22*, e51121. https://doi.org/10.15252/embr.202051121.

29. Xu, L., Ajimura, M., Padmore, R., Klein, C., and Kleckner, N. (1995). NDT80, a meiosis-specific gene required for exit from pachytene in Saccharomyces cerevisiae. Mol. Cell. Biol. *15*, 6572–6581. https://doi.org/10.1128/MCB.15.12.6572.

30. Lee, B.H., and Amon, A. (2003). Role of Polo-like kinase CDC5 in programming meiosis I chromosome segregation. Science *300*, 482–486. https://doi.org/10.1126/science.1081846.

31. Ludwig, C., Gillet, L., Rosenberger, G., Amon, S., Collins, B.C., and Aebersold, R. (2018). Data-independent acquisition-based SWATH-MS for quantitative proteomics: a tutorial. Mol. Syst. Biol. *14*, e8126. https://doi.org/10.15252/msb.20178126.

32. Gillet, L.C., Navarro, P., Tate, S., Röst, H., Selevsek, N., Reiter, L., Bonner, R., and Aebersold, R. (2012). Targeted data extraction of the MS/MS spectra generated by data-independent acquisition: a new concept for consistent and accurate proteome analysis. Mol. Cell. Proteomics *11*, O111.016717. https://doi.org/10.1074/mcp.O111.016717.

33. Schubert, O.T., Gillet, L.C., Collins, B.C., Navarro, P., Rosenberger, G., Wolski, W.E., Lam, H., Amodei, D., Mallick, P., MacLean, B., and Aebersold, R. (2015). Building high-quality assay libraries for targeted analysis of SWATH MS data. Nat. Protoc. *10*, 426–441. https://doi.org/10.1038/nprot.2015.015.

34. Ho, B., Baryshnikova, A., and Brown, G.W. (2018). Unification of protein abundance datasets yields a quantitative Saccharomyces cerevisiae proteome. Cell Syst. *6*, 192–205.e3. https://doi.org/10.1016/j.cels.2017.12.004.

35. Grossbach, J., Gillet, L., Clément-Ziza, M., Schmalohr, C.L., Schubert, O.T., Schütter, M., Mawer, J.S.P., Barnes, C.A., Bludau, I., Weith, M., et al. (2022). The impact of genomic variation on protein phosphorylation states and regulatory networks. Mol. Syst. Biol. *18*, e10712. https://doi.org/10.15252/msb.202110712.

36. Stark, C., Breitkreutz, B.J., Reguly, T., Boucher, L., Breitkreutz, A., and Tyers, M. (2006). BioGRID: a general repository for interaction datasets. Nucleic Acids Res. *34*, D535–D539. https://doi.org/10.1093/nar/gkj109.

37. Hernandez-Armenta, C., Ochoa, D., Gonçalves, E., Saez-Rodriguez, J., and Beltrao, P. (2017). Benchmarking substrate-based kinase activity inference using phosphoproteomic data. Bioinformatics *33*, 1845–1851. https://doi.org/10.1093/bioinformatics/btx082.

38. Kumar, L., and E Futschik, M. (2007). Mfuzz: a software package for soft clustering of microarray data. Bioinformation *2*, 5–7. https://doi.org/10.6026/97320630002005.

39. Carlile, T.M., and Amon, A. (2008). Meiosis I is established through division-specific translational control of a cyclin. Cell *133*, 280–291. https://doi.org/10.1016/j.cell.2008.02.032.

40. Benjamin, K.R., Zhang, C., Shokat, K.M., and Herskowitz, I. (2003). Control of landmark events in meiosis by the CDK Cdc28 and the meiosis-specific kinase Ime2. Genes Dev. *17*, 1524–1539. https://doi.org/10.1101/gad.1101503.

41. Clyne, R.K., Katis, V.L., Jessop, L., Benjamin, K.R., Herskowitz, I., Lichten, M., and Nasmyth, K. (2003). Polo-like kinase Cdc5 promotes chiasmata formation and cosegregation of sister centromeres at meiosis I. Nat. Cell Biol. *5*, 480–485. https://doi.org/10.1038/ncb977.

42. Holt, L.J., Hutti, J.E., Cantley, L.C., and Morgan, D.O. (2007). Evolution of Ime2 phosphorylation sites on Cdk1 substrates provides a mechanism to limit the effects of the phosphatase Cdc14 in meiosis. Mol. Cell *25*, 689–702. https://doi.org/10.1016/j.molcel.2007.02.012.

43. Mok, J., Kim, P.M., Lam, H.Y.K., Piccirillo, S., Zhou, X., Jeschke, G.R., Sheridan, D.L., Parker, S.A., Desai, V., Jwa, M., et al. (2010). Deciphering protein kinase specificity through large-scale analysis of yeast phosphorylation site motifs. Sci. Signal. *3*, ra12. https://doi.org/10.1126/scisignal.2000482.

44. Argüello-Miranda, O., Zagoriy, I., Mengoli, V., Rojas, J., Jonak, K., Oz, T., Graf, P., and Zachariae, W. (2017). Casein kinase 1 coordinates cohesin cleavage, gametogenesis, and exit from M phase in meiosis II. Dev. Cell *40*, 37–52. https://doi.org/10.1016/j.devcel.2016.11.021.

45. Pu, S., Wong, J., Turner, B., Cho, E., and Wodak, S.J. (2009). Up-to-date catalogues of yeast protein complexes. Nucleic Acids Res. *37*, 825–831. https://doi.org/10.1093/nar/gkn1005.

46. Song, J., Pfanner, N., and Becker, T. (2018). Assembling the mitochondrial ATP synthase. Proc. Natl. Acad. Sci. USA *115*, 2850–2852. https://doi.org/10.1073/pnas.1801697115.

47. Matos, J., Lipp, J.J., Bogdanova, A., Guillot, S., Okaz, E., Junqueira, M., Shevchenko, A., and Zachariae, W. (2008). Dbf4-dependent CDC7 kinase links DNA replication to the segregation of homologous chromosomes in meiosis I. Cell *135*, 662–678. https://doi.org/10.1016/j.cell.2008.10.026.

48. Galander, S., Barton, R.E., Borek, W.E., Spanos, C., Kelly, D.A., Robertson, D., Rappsilber, J., and Marston, A.L. (2019). Reductional meiosis I chromosome segregation is established by coordination of key meiotic kinases. Dev. Cell *49*, 526–541.e5. https://doi.org/10.1016/j.devcel.2019.04.003.

49. Zickler, D., and Kleckner, N. (2015). Recombination, pairing, and Synapsis of homologs during meiosis. Cold Spring Harbor Perspect. Biol. *7*, a016626. https://doi.org/10.1101/cshperspect.a016626.

50. Hunter, N. (2015). Meiotic recombination: the essence of heredity. Cold Spring Harbor Perspect. Biol. *7*, a016618. https://doi.org/10.1101/cshperspect.a016618.

51. Chen, X., Suhandynata, R.T., Sandhu, R., Rockmill, B., Mohibullah, N., Niu, H., Liang, J., Lo, H.C., Miller, D.E., Zhou, H., et al. (2015). Phosphorylation of the synaptonemal complex protein Zip1 regulates the crossover/noncrossover decision during yeast meiosis. PLOS Biol. *13*, e1002329. https://doi.org/10.1371/journal.pbio.1002329.

52. Carballo, J.A., Johnson, A.L., Sedgwick, S.G., and Cha, R.S. (2008). Phosphorylation of the axial element protein Hop1 by Mec1/Tel1 ensures meiotic interhomolog recombination. Cell *132*, 758–770. https://doi.org/10.1016/j.cell.2008.01.035.

53. Jordan, P., Copsey, A., Newnham, L., Kolar, E., Lichten, M., and Hoffmann, E. (2009). Ipl1/aurora B kinase coordinates synaptonemal complex disassembly with cell cycle progression and crossover formation in budding yeast meiosis. Genes Dev. *23*, 2237–2251. https://doi.org/10.1101/gad.536109.

54. Argunhan, B., Leung, W.K., Afshar, N., Terentyev, Y., Subramanian, V.V., Murayama, Y., Hochwagen, A., Iwasaki, H., Tsubouchi, T., and Tsubouchi, H. (2017). Fundamental cell cycle kinases collaborate to ensure timely destruction of the synaptonemal complex during meiosis. EMBO J. *36*, 2488–2509. https://doi.org/10.15252/embj.201695895.

55. Hollingsworth, N.M., Ponte, L., and Halsey, C. (1995). MSH5, a novel MutS homolog, facilitates meiotic reciprocal recombination between homologs in Saccharomyces cerevisiae but not mismatch repair. Genes Dev. *9*, 1728–1739. https://doi.org/10.1101/gad.9.14.1728.

56. He, W., Rao, H.B.D.P., Tang, S., Bhagwat, N., Kulkarni, D.S., Ma, Y., Chang, M.A.W., Hall, C., Bragg, J.W., Manasca, H.S., et al. (2020). Regulated proteolysis of MutSgamma controls meiotic crossing over. Mol. Cell *78*, 168–183.e5. https://doi.org/10.1016/j.molcel.2020.02.001.

57. Kühlbrandt, W. (2019). Structure and mechanisms of F-type ATP synthases. Annu. Rev. Biochem. *88*, 515–549. https://doi.org/10.1146/annurev-biochem-013118-110903.

58. Reinders, J., Wagner, K., Zahedi, R.P., Stojanovski, D., Eyrich, B., van der Laan, M., Rehling, P., Sickmann, A., Pfanner, N., and Meisinger, C. (2007). Profiling phosphoproteins of yeast mitochondria reveals a role of phosphorylation in assembly of the ATP synthase. Mol. Cell. Proteomics *6*, 1896–1906. https://doi.org/10.1074/mcp.M700098-MCP200.

59. Zaman, S., Lippman, S.I., Zhao, X., and Broach, J.R. (2008). How Saccharomyces responds to nutrients. Annu. Rev. Genet. *42*, 27–81. https://doi.org/10.1146/annurev.genet.41.110306.130206.

60. Hugener, J., Xu, J., Wettstein, R., Ioannidi, L., Velikov, D., Wollweber, F., Henggeler, A., Matos, J., and Pilhofer, M. (2023). FilamentID reveals the composition and function of metabolic enzyme polymers during gametogenesis. Cell *187*, 3303–3318. https://doi.org/10.1016/j.cell.2024.04.026.

61. Beck, M., and Baumeister, W. (2016). Cryo-electron tomography: can it reveal the molecular sociology of cells in atomic detail? Trends Cell Biol. *26*, 825–837. https://doi.org/10.1016/j.tcb.2016.08.006.

62. Zachs, T., Schertel, A., Medeiros, J., Weiss, G.L., Hugener, J., Matos, J., and Pilhofer, M. (2020). Fully automated, sequential focused ion beam milling for cryo-electron tomography. eLife *9*, e52286. https://doi.org/10.7554/eLife.52286.

63. Gorsich, S.W., and Shaw, J.M. (2004). Importance of mitochondrial dynamics during meiosis and sporulation. Mol. Biol. Cell *15*, 4369–4381. https://doi.org/10.1091/mbc.e03-12-0875.

64. Morgenstern, M., Stiller, S.B., Lübbert, P., Peikert, C.D., Dannenmaier, S., Drepper, F., Weill, U., Höß, P., Feuerstein, R., Gebert, M., et al. (2017). Definition of a high-confidence mitochondrial proteome at quantitative scale. Cell Rep. *19*, 2836–2852. https://doi.org/10.1016/j.celrep.2017.06.014.

65. Jumper, J., Evans, R., Pritzel, A., Green, T., Figurnov, M., Ronneberger, O., Tunyasuvunakool, K., Bates, R., Žídek, A., Potapenko, A., et al. (2021). Highly accurate protein structure prediction with AlphaFold. Nature *596*, 583–589. https://doi.org/10.1038/s41586-021-03819-2.

66. Varadi, M., Anyango, S., Deshpande, M., Nair, S., Natassia, C., Yordanova, G., Yuan, D., Stroe, O., Wood, G., Laydon, A., et al. (2022). AlphaFold Protein Structure Database: massively expanding the structural coverage of protein-sequence space with high-accuracy models. Nucleic Acids Res. *50*, D439–D444. https://doi.org/10.1093/nar/gkab1061.

67. Perez-Miller, S.J., and Hurley, T.D. (2003). Coenzyme isomerization is integral to catalysis in aldehyde dehydrogenase. Biochemistry *42*, 7100–7109. https://doi.org/10.1021/bi034182w.

68. Hill, R.J., and Crossan, G.P. (2019). DNA cross-link repair safeguards genomic stability during premeiotic germ cell development. Nat. Genet. *51*, 1283–1294. https://doi.org/10.1038/s41588-019-0471-2.

69. Beltrao, P., Bork, P., Krogan, N.J., and van Noort, V. (2013). Evolution and functional cross-talk of protein post-translational modifications. Mol. Syst. Biol. *9*, 714. https://doi.org/10.1002/msb.201304521.

70. Millar, A.H., Heazlewood, J.L., Giglione, C., Holdsworth, M.J., Bachmair, A., and Schulze, W.X. (2019). The scope, functions, and dynamics of posttranslational protein modifications. Annu. Rev. Plant Biol. *70*, 119–151. https://doi.org/10.1146/annurev-arplant-050718-100211.

71. Galander, S., and Marston, A.L. (2020). Meiosis I kinase regulators: conserved orchestrators of reductional chromosome segregation. Bioessays *42*, e2000018. https://doi.org/10.1002/bies.202000018.

72. Miyakawa, I., Aoi, H., Sando, N., and Kuroiwa, T. (1984). Fluorescence microscopic studies of mitochondrial nucleoids during meiosis and sporulation in the yeast, Saccharomyces cerevisiae. J. Cell Sci. *66*, 21–38. https://doi.org/10.1242/jcs.66.1.21.

73. Sawyer, E.M., Joshi, P.R., Jorgensen, V., Yunus, J., Berchowitz, L.E., and Ünal, E. (2019). Developmental regulation of an organelle tether coordinates mitochondrial remodeling in meiosis. J. Cell Biol. *218*, 559–579. https://doi.org/10.1083/jcb.201807097.

74. Noree, C., and Sirinonthanawech, N. (2020). Coupled regulations of enzymatic activity and structure formation of aldehyde dehydrogenase Ald4p. Biol. Open *9*, bio051110. https://doi.org/10.1242/bio.051110.

75. Misonou, Y., Kikuchi, M., Sato, H., Inai, T., Kuroiwa, T., Tanaka, K., and Miyakawa, I. (2014). Aldehyde dehydrogenase, Ald4p, is a major component of mitochondrial fluorescent inclusion bodies in the yeast Saccharomyces cerevisiae. Biol. Open *3*, 387–396. https://doi.org/10.1242/bio.20147138.

76. Vasiliou, V., and Nebert, D.W. (2005). Analysis and update of the human aldehyde dehydrogenase (ALDH) gene family. Hum. Genomics *2*, 138–143. https://doi.org/10.1186/1479-7364-2-2-138.

77. Gross, E.R., Zambelli, V.O., Small, B.A., Ferreira, J.C.B., Chen, C.H., and Mochly-Rosen, D. (2015). A personalized medicine approach for Asian Americans with the aldehyde dehydrogenase 2*2 variant. Annu. Rev. Pharmacol. Toxicol. *55*, 107–127. https://doi.org/10.1146/annurev-pharmtox-010814-124915.

78. Shortall, K., Djeghader, A., Magner, E., and Soulimane, T. (2021). Insights into aldehyde dehydrogenase enzymes: A structural perspective. Front. Mol. Biosci. *8*, 659550. https://doi.org/10.3389/fmolb.2021.659550.

79. Beltrao, P., Albanèse, V., Kenner, L.R., Swaney, D.L., Burlingame, A., Villén, J., Lim, W.A., Fraser, J.S., Frydman, J., and Krogan, N.J. (2012). Systematic functional prioritization of protein posttranslational modifications. Cell *150*, 413–425. https://doi.org/10.1016/j.cell.2012.05.036.

80. Ochoa, D., Jarnuczak, A.F., Viéitez, C., Gehre, M., Soucheray, M., Mateus, A., Kleefeldt, A.A., Hill, A., Garcia-Alonso, L., Stein, F., et al. (2020). The functional landscape of the human phosphoproteome. Nat. Biotechnol. *38*, 365–373. https://doi.org/10.1038/s41587-019-0344-3.

81. Nishi, H., Hashimoto, K., and Panchenko, A.R. (2011). Phosphorylation in protein-protein binding: effect on stability and function. Structure *19*, 1807–1815. https://doi.org/10.1016/j.str.2011.09.021.

82. Betts, M.J., Wichmann, O., Utz, M., Andre, T., Petsalaki, E., Minguez, P., Parca, L., Roth, F.P., Gavin, A.C., Bork, P., and Russell, R.B. (2017). Systematic identification of phosphorylation-mediated protein interaction switches. PLoS Comput. Biol. *13*, e1005462. https://doi.org/10.1371/journal.pcbi.1005462.

83. Onischenko, E., Stanton, L.H., Madrid, A.S., Kieselbach, T., and Weis, K. (2009). Role of the Ndc1 interaction network in yeast nuclear pore complex assembly and maintenance. J. Cell Biol. *185*, 475–491. https://doi.org/10.1083/jcb.200810030.

84. Gerhardy, S., Oborská-Oplová, M., Gillet, L., Börner, R., van Nues, R., Leitner, A., Michel, E., Petkowski, J.J., Granneman, S., Sigel, R.K.O., et al. (2021). Puf6 primes 60S pre-ribosome nuclear export at low temperature. Nat. Commun. *12*, 4696. https://doi.org/10.1038/s41467-021-24964-2.

85. Grigaitis, R., Ranjha, L., Wild, P., Kasaciunaite, K., Ceppi, I., Kissling, V., Henggeler, A., Susperregui, A., Peter, M., Seidel, R., et al. (2020). Phosphorylation of the RecQ helicase Sgs1/BLM controls its DNA unwinding activity during meiosis and mitosis. Dev. Cell *53*, 706–723.e5. https://doi.org/10.1016/j.devcel.2020.05.016.

86. Yates, A., Akanni, W., Amode, M.R., Barrell, D., Billis, K., Carvalho-Silva, D., Cummins, C., Clapham, P., Fitzgerald, S., Gil, L., et al. (2016). Ensembl 2016. Nucleic Acids Res. *44*, D710–D716. https://doi.org/10.1093/nar/gkv1157.

87. Chatr-Aryamontri, A., Oughtred, R., Boucher, L., Rust, J., Chang, C., Kolas, N.K., O'Donnell, L., Oster, S., Theesfeld, C., Sellam, A., et al. (2017). The BioGRID interaction database: 2017 update. Nucleic Acids Res. *45*, D369–D379. https://doi.org/10.1093/nar/gkw1102.

88. Schindelin, J., Arganda-Carreras, I., Frise, E., Kaynig, V., Longair, M., Pietzsch, T., Preibisch, S., Rueden, C., Saalfeld, S., Schmid, B., et al. (2012). Fiji: an open-source platform for biological-image analysis. Nat. Methods *9*, 676–682. https://doi.org/10.1038/nmeth.2019.

89. Röst, H.L., Rosenberger, G., Navarro, P., Gillet, L., Miladinović, S.M., Schubert, O.T., Wolski, W., Collins, B.C., Malmström, J., Malmström, L., and Aebersold, R. (2014). OpenSWATH enables automated, targeted analysis of data-independent acquisition MS data. Nat. Biotechnol. *32*, 219–223. https://doi.org/10.1038/nbt.2841.

90. Teleman, J., Röst, H.L., Rosenberger, G., Schmitt, U., Malmström, L., Malmström, J., and Levander, F. (2015). Diana–algorithmic improvements for analysis of data-independent acquisition MS data. Bioinformatics *31*, 555–562. https://doi.org/10.1093/bioinformatics/btu686.

91. Gu, Z., Eils, R., and Schlesner, M. (2016). Complex heatmaps reveal patterns and correlations in multidimensional genomic data. Bioinformatics *32*, 2847–2849. https://doi.org/10.1093/bioinformatics/btw313.

92. Durinck, S., Spellman, P.T., Birney, E., and Huber, W. (2009). Mapping identifiers for the integration of genomic datasets with the R/Bioconductor package biomaRt. Nat. Protoc. *4*, 1184–1191. https://doi.org/10.1038/nprot.2009.97.

93. Ou, J., Liu, H., Nirala, N.K., Stukalov, A., Acharya, U., Green, M.R., and Zhu, L.J. (2020). dagLogo: an R/Bioconductor package for identifying and visualizing differential amino acid group usage in proteomics data. PloS One *15*, e0242030. https://doi.org/10.1371/journal.pone.0242030.

94. Wagih, O. (2017). ggseqlogo: a versatile R package for drawing sequence logos. Bioinformatics *33*, 3645–3647. https://doi.org/10.1093/bioinformatics/btx469.

95. Mastronarde, D.N. (2005). Automated electron microscope tomography using robust prediction of specimen movements. J. Struct. Biol. *152*, 36–51. https://doi.org/10.1016/j.jsb.2005.07.007.

96. Kremer, J.R., Mastronarde, D.N., and McIntosh, J.R. (1996). Computer visualization of three-dimensional image data using IMOD. J. Struct. Biol. *116*, 71–76. https://doi.org/10.1006/jsbi.1996.0013.

97. Pettersen, E.F., Goddard, T.D., Huang, C.C., Meng, E.C., Couch, G.S., Croll, T.I., Morris, J.H., and Ferrin, T.E. (2021). UCSF ChimeraX: structure visualization for researchers, educators, and developers. Protein Sci. *30*, 70–82. https://doi.org/10.1002/pro.3943.

98. Matos, J., Blanco, M.G., Maslen, S., Skehel, J.M., and West, S.C. (2011). Regulatory control of the resolution of DNA recombination intermediates during meiosis and mitosis. Cell *147*, 158–172. https://doi.org/10.1016/j.cell.2011.08.032.

99. Chen, P.L., Chen, C.F., Chen, Y., Xiao, J., Sharp, Z.D., and Lee, W.H. (1998). The BRC repeats in BRCA2 are critical for RAD51 binding and resistance to methyl methanesulfonate treatment. Proc. Natl. Acad. Sci. USA *95*, 5287–5292. https://doi.org/10.1073/pnas.95.9.5287.

100. Knop, M., Siegers, K., Pereira, G., Zachariae, W., Winsor, B., Nasmyth, K., and Schiebel, E. (1999). Epitope tagging of yeast genes using a PCR-based strategy: more tags and improved practical routines. Yeast *15*, 963–972. https://doi.org/10.1002/(SICI)1097-0061(199907)15:10B<963::AID-YEA399>3.0.CO;2-W.

101. Giaever, G., Chu, A.M., Ni, L., Connelly, C., Riles, L., Véronneau, S., Dow, S., Lucau-Danila, A., Anderson, K., André, B., et al. (2002). Functional profiling of the Saccharomyces cerevisiae genome. Nature *418*, 387–391. https://doi.org/10.1038/nature00935.

102. Grigaitis, R., Susperregui, A., Wild, P., and Matos, J. (2018). Characterization of DNA helicases and nucleases from meiotic extracts of S. cerevisiae. Methods Cell Biol. *144*, 371–388. https://doi.org/10.1016/bs.mcb.2018.03.029.

103. Wild, P., Susperregui, A., Piazza, I., Dörig, C., Oke, A., Arter, M., Yamaguchi, M., Hilditch, A.T., Vuina, K., Chan, K.C., et al. (2019). Network rewiring of homologous recombination enzymes during mitotic proliferation and meiosis. Mol. Cell *75*, 859–874.e4. https://doi.org/10.1016/j.molcel.2019.06.022.

104. Salah, S.M., and Nasmyth, K. (2000). Destruction of the securin Pds1p occurs at the onset of anaphase during both meiotic divisions in yeast. Chromosoma *109*, 27–34. https://doi.org/10.1007/s004120050409.

105. Loidl, J., Klein, F., and Engebrecht, J. (1998). Genetic and morphological approaches for the analysis of meiotic chromosomes in yeast. Methods Cell Biol. *53*, 257–285. https://doi.org/10.1016/s0091-679x(08)60882-1.

106. Keller, A., Nesvizhskii, A.I., Kolker, E., and Aebersold, R. (2002). Empirical statistical model to estimate the accuracy of peptide identifications made by MS/MS and database search. Anal. Chem. *74*, 5383–5392. https://doi.org/10.1021/ac025747h.

107. Shteynberg, D., Deutsch, E.W., Lam, H., Eng, J.K., Sun, Z., Tasman, N., Mendoza, L., Moritz, R.L., Aebersold, R., and Nesvizhskii, A.I. (2011). iProphet: multi-level integrative analysis of shotgun proteomic data improves peptide and protein identification rates and error estimates. Mol. Cell. Proteomics *10*, M111.007690. https://doi.org/10.1074/mcp.M111.007690.

108. Lam, H., Deutsch, E.W., Eddes, J.S., Eng, J.K., Stein, S.E., and Aebersold, R. (2008). Building consensus spectral libraries for peptide identification in proteomics. Nat. Methods *5*, 873–875. https://doi.org/10.1038/nmeth.1254.

109. Navarro, P., Kuharev, J., Gillet, L.C., Bernhardt, O.M., MacLean, B., Röst, H.L., Tate, S.A., Tsou, C.C., Reiter, L., Distler, U., et al. (2016). A multicenter study benchmarks software tools for label-free proteome quantification. Nat. Biotechnol. *34*, 1130–1136. https://doi.org/10.1038/nbt.3685.

110. Huang da, W., Sherman, B.T., and Lempicki, R.A. (2009). Systematic and integrative analysis of large gene lists using David bioinformatics resources. Nat. Protoc. *4*, 44–57. https://doi.org/10.1038/nprot.2008.211.

111. Engel, S.R., Dietrich, F.S., Fisk, D.G., Binkley, G., Balakrishnan, R., Costanzo, M.C., Dwight, S.S., Hitz, B.C., Karra, K., Nash, R.S., et al. (2014). The reference genome sequence of Saccharomyces cerevisiae: then and now. G3 (Bethesda) *4*, 389–398. https://doi.org/10.1534/g3.113.008995.

112. Bodenmiller, B., Wanka, S., Kraft, C., Urban, J., Campbell, D., Pedrioli, P.G., Gerrits, B., Picotti, P., Lam, H., Vitek, O., et al. (2010). Phosphoproteomic analysis reveals interconnected system-wide responses to perturbations of kinases and phosphatases in yeast. Sci. Signal. *3*, rs4. https://doi.org/10.1126/scisignal.2001182.

113. Iancu, C.V., Tivol, W.F., Schooler, J.B., Dias, D.P., Henderson, G.P., Murphy, G.E., Wright, E.R., Li, Z., Yu, Z., Briegel, A., et al. (2006). Electron cryotomography sample preparation using the Vitrobot. Nat. Protoc. *1*, 2813–2819. https://doi.org/10.1038/nprot.2006.432.

114. Tivol, W.F., Briegel, A., and Jensen, G.J. (2008). An improved cryogen for plunge freezing. Microsc. Microanal. *14*, 375–379. https://doi.org/10.1017/S1431927608080781.

115. Medeiros, J.M., Böck, D., Weiss, G.L., Kooger, R., Wepf, R.A., and Pilhofer, M. (2018). Robust workflow and instrumentation for cryo-focused ion beam milling of samples for electron cryotomography. Ultramicroscopy *190*, 1–11. https://doi.org/10.1016/j.ultramic.2018.04.002.

116. Tegunov, D., and Cramer, P. (2019). Real-time cryo-electron microscopy data preprocessing with Warp. Nat. Methods *16*, 1146–1152. https://doi.org/10.1038/s41592-019-0580-y.

STAR★METHODS

KEY RESOURCES TABLE

REAGENT or RESOURCE	SOURCE	IDENTIFIER
Antibodies		
Mouse anti-GFP IgG	Roche	Cat#11814460001; RRID: AB_390913
Rabbit anti-Ald4	This study	N/A
Mouse anti-Cdc5	Médimabs	Cat#MM-0192-1-100
Rabbit anti-Myc HRP	Abcam	Cat#ab1326; RRID: AB_299800
Mouse anti-Flag HRP	Sigma Aldrich	Cat#A8592-1MG; RRID: AB_439702
Rabbit anti-Crm1	K. Weis (ETH Zurich)	not commercial, no RRID. Onischenko et al.[83]
Rabbit anti-Puf6	V. Panse (University of Zurich)	Not commercial, no RRID. Gerhardy et al.[84]
Rat anti-α-tubulin	Biorad	Cat# MCA78G; RRID: AB_325005
Rabbit anti-Zip1	J. Matos (University of Vienna)	Not commercial, no RRID Grigaitis et al.[85]
Mouse anti-mCherry	Clontech Takara	Cat#632543; RRID: AB_2307319
Goat anti-Mouse IgG (HRP)	Agilent	Cat#P0447; RRID: AB_2617137
Swine anti-Rabbit IgG (HRP)	Agilent	Cat#P0399; RRID: AB_2617141
Donkey anti-rabbit Alexa fluor 488	Thermo Fisher Scientific	Cat#A-21206; RRID: AB_2535792
Donkey anti-mouse Alexa fluor 555	Thermo Fisher Scientific	Cat#A-31570; RRID: AB_2536180
Chicken anti-rat Alexa fluor 647	Thermo Fisher Scientific	Cat#A-21472; RRID: AB_1500700
Chemicals, peptides, and recombinant proteins		
Trypsin, sequencing grade	Promega	Cat#V5111
Sep-Pak C18 3cc Vac RC cartridge	Waters	Cat#WAT036945
TiO_2 resin	GL Science	Cat#5020-75000
C18 Micro Spin Columns	The Nest group	Cat#74-4601
iRT reference peptides	Biognosys	Cat#Ki-3002-1
Magic C18 AQ 3 μm resin	Michrom BioResources	N/A
Bio-Rad Protein Assay	Bio-Rad	Cat#5000006
NuPAGE™ sample buffer	Thermo Fisher Scientific	Cat#NP0008
NativePAGE sample buffer (4X)	Thermo Fisher Scientific	Cat#BN2003
Tris Acetate running buffer (20X)	Thermo Fisher Scientific	Cat#LA0041
MES running buffer (20X)	Thermo Fisher Scientific	Cat#NP0002
NativePAGE Running buffer (20X)	Thermo Fisher Scientific	Cat#BN2001
BioRad Precision Plus Protein Dual Color Standard	BioRad	Cat#1610374
NativeMark Unstained Protein Standard	Thermo Fisher Scientific	Cat#LC0725
RNase A	Roche	Cat#10109169001
Propidium Iodide	Sigma Aldrich	Cat#81845
ProLong™ Diamond Antifade Mountant with DAPI	Thermo Fisher Scientific	Cat#P36962
Zymolyase 20T	Seikagaku Biobusiness	Cat#120491
Zymolyase 100T	Seikagaku Biobusiness	Cat#120493-1
λ-phosphatase	NEB	Cat#P0753S
cOmplete™, EDTA-free Protease Inhibitor Cocktail	Roche	Cat#05056489001
Anti-Myc agarose beads (9E10)	Cancer Research UK	N/A
Phos-Tag Acrylamide	Wako chemicals	Cat#AAL-107
Di(N-succinimidyl) glutarate	Sigma-Aldrich	Cat#80424
Protein A - 10nm Gold Conjugate	Cryodiagnostics	Cat#AC-10-05-05

(*Continued on next page*)

Continued

REAGENT or RESOURCE	SOURCE	IDENTIFIER
Deposited data		
Yeast reference genome SGD DB release 13.1.2015	SGD database	http://sgd-archive.yeastgenome.org/sequence/S288C_reference/genome_releases/
BioGRID_post translational modifications	BioGRID repository[36]	https://wiki.thebiogrid.org/doku.php/tools
GO-term entries Ensemble DB V86	Ensemble database[86]	http://www.ensembl.org/Help/View?id=285
BioGRID_substrate-kinase predictions	BioGRID repository[87]	https://wiki.thebiogrid.org/doku.php/tools
Protein Complex list	Wodak lab[45]	http://wodaklab.org/cyc2008/
Mass Spectrometry datasets	This study ProteomeXchange/PRIDE	ProteomeXchange/PRIDE PXD033675
Cryo-tomogram of FIB-milled vegetatively growing yeast cell with mitochondria	This study	EMDB: EMD-50229
Cryo-tomogram of FIB-milled pre-meiotic yeast cell with mitochondria	This study	EMDB: EMD-50230
Cryo-tomogram of FIB-milled meiotic yeast cell containing mitochondria with filaments	This study	EMDB: EMD-50231
Cryo-tomogram of FIB-milled yeast spore with mitochondria	This study	EMDB: EMD-50232
Cryo-tomogram of FIB-milled meiotic yeast cell containing mitochondria with filament arrays	This study	EMDB: EMD-50233
Cryo-tomogram of purified meiotic yeast mitochondria with Ald4 filaments	This study	EMDB: EMD-50234
Raw data for all Western Blots, Spot assays and Immunofluorescence images displayed in the study	This study	Mendeley Data: https://doi.org/10.17632/d4kcp9zvkj.1
Experimental models: Organisms/strains		
All strains used in this study are listed in Table S4	This study	N/A
Recombinant DNA		
YIpLac128-*ALD4*^{WT}	This study	pML767
YIpLac128-*ald4*^{3A}	This study	pML818
Software and algorithms		
Fiji (Fiji Is Just ImageJ)	Schindelin et al.[88]	https://fiji.sc/
Prism 9	GraphPad	https://www.graphpad.com/
FlowJo v10	Becton Dickinson	https://www.bdbiosciences.com/en-ch/products/software/flowjo-v10-software
Msconvert Proteowizzard v3.0.9987	Proteowizzard	https://proteowizard.sourceforge.io/projects.html
TPP v4.7 re0 COMET 2014.02 rev.0	Sourceforge	https://sourceforge.net/projects/sashimi/files/Trans-Proteomic%20Pipeline%20%28TPP%29/
TPP v4.7 re0 Mascot v2.5.1	Sourceforge	https://sourceforge.net/projects/sashimi/files/Trans-Proteomic%20Pipeline%20%28TPP%29/
TPP v4.7 re0 PeptideProphet	Sourceforge	https://sourceforge.net/projects/sashimi/files/Trans-Proteomic%20Pipeline%20%28TPP%29/
TPP v4.7 re0 iProphet	Sourceforge	https://sourceforge.net/projects/sashimi/files/Trans-Proteomic%20Pipeline%20%28TPP%29/
TPP v4.7 re0 Spectrast2tsv.py	Sourceforge	https://sourceforge.net/projects/sashimi/files/Trans-Proteomic%20Pipeline%20%28TPP%29/

(*Continued on next page*)

Continued

REAGENT or RESOURCE	SOURCE	IDENTIFIER
openSWATH (openMS 2.1.0)	Rost et al.[89]	http://openswath.org/en/latest/
pyProphet	Teleman et al.[90]	https://pypi.python.org/pypi/pyprophet
TRIC alignment	Rost et al.[89]	https://pypi.org/project/msproteomicstools/
ComplexHeatmap R package version 2.0.0	Gu et al.[91]	https://bioconductor.org/packages/release/bioc/html/ComplexHeatmap.html
biomaRT R package version 2.38.0	Durinck et al.[92]	https://bioconductor.org/packages/release/bioc/html/biomaRt.html
DagLogo R package	Ou et al.[93]	https://www.bioconductor.org/packages/release/bioc/html/dagLogo.html
Ggseqlogo R package	Wagih[94]	https://omarwagih.github.io/ggseqlogo/
SerialEM	Mastronarde[95]	https://bio3d.colorado.edu/SerialEM/
IMOD	Kremer et al.[96]	https://bio3d.colorado.edu/imod/
UCSF ChimeraX	Pettersen et al.[97]	https://www.rbvi.ucsf.edu/chimerax//
Other		
Nunc™ Lab-Tek™ II Chambered Coverglass	Thermo Fisher Scientific	Cat#155409
NuPAGE™ Novex™ 3-8%, Tris-Acetate Midi gels	Thermo Fisher Scientific	Cat#WG1602BOX
NuPAGE™ Novex™ 4-12% Bis-Tris Midi gels	Thermo Fisher Scientific	Cat#WG1402BOX
NativePAGE™ Novex™ 4-16% Bis-Tris Gels	Thermo Fisher Scientific	Cat#BN1002BOX
Amersham™ Hybond™ P 0.45 PVDF blotting membrane	Cytiva	Cat#GE10600023
DeltaVision Ultra Epifluorescence Microscope	Image Solutions	N/A
ChemiDoc MP	Bio-Rad	N/A
FastPrep-24	MP Biomedicals	N/A
FACSCalibur or FACSCanto	Becton Dickinson	N/A
5600 Sciex Triple TOF mass spectrometer (Eksigent NanoLC Ultra 1D Plus system interface)	Sciex	N/A
6600 Sciex Triple TOF mass spectrometer (Eksigent NanoLC Ultra 1D Plus system interface)	Sciex	N/A
Copper EM grids (R2/2 200 mesh, R2/1 200 mesh)	Quantifoil	https://www.quantifoil.com
Vitrobot Mark IV	Thermo Fisher Scientific	N/A
Crossbeam 550 FIB-SEM	Zeiss	N/A
Cryo-transmission electron microscope Titan Krios (300kV)	Thermo Fisher Scientific	N/A

RESOURCE AVAILABILITY

Lead contact

Further information and requests for resources and reagents should be directed to and will be fulfilled by the lead contact, Joao Matos (joao.matos@maxperutzlabs.ac.at).

Materials availability

Plasmids and yeast strains generated in this study are available upon request from the lead contact.

Data and code availability

The mass spectrometry proteomics data have been deposited to the ProteomeXchange consortium via the PRIDE partner repository with the dataset identifier PXD033675 and are publicly available as of the date of publication.

Example cryo-tomograms shown in the main figures have been deposited to the Electron Microscopy Data Bank (EMDB). The EMDB entries for the cryo-tomograms are: EMD-50229 (FIB-milled vegetatively growing yeast cell with mitochondria), EMD-50230 (FIB-milled pre-meiotic yeast cell with mitochondria), EMD-50231 (FIB-milled meiotic yeast cell containing mitochondria with filaments), EMD-50232 (FIB-milled yeast spore with mitochondria), EMD-50233 (FIB-milled meiotic yeast cell containing mitochondria with filament arrays) and EMD-50234 (purified meiotic yeast mitochondria with Ald4 filaments). All tomograms are publicly available as of the date of publication.

Raw data from Figures 3, 4, 5, S4, and S6 has been deposited on Mendeley, https://doi.org/10.17632/d4kcp9zvkj.1 and will be publicly available as of the date of publication. DOIs are listed in the key resources table

The paper does not report original code. Any additional information required to reanalyze the data reported in this paper is available from the lead contact upon request.

EXPERIMENTAL MODEL AND STUDY PARTICIPANT DETAILS

Saccharomyces cerevisiae

All budding yeast strains used in this study are SK1 derivates. They were cultured under standard conditions at 30 °C in YPD (yeast extract 1%, peptone 2%, dextrose 2%) either as liquid culture or on agar plates unless otherwise indicated. Details are specified in Table S4. All experiments were carried out in diploid strain backgrounds.

METHOD DETAILS

Strain generation

All yeast strains used are SK1 derivatives. Details are specified in Table S4. The following alleles have been describe previously: *ndt80Δ*,[98] *cdc20*^{mn}.[99] For C-terminal epitope tagging of chromosomal genes, Myc9, 6xHis6Flag and 3xmCherry cassettes were amplified from plasmids by PCR as described.[100] Gene deletions were introduced directly in SK1 background by PCR-based amplification of deletion cassettes from a yeast knock-out collection.[101] Point mutations were introduced by mutagenic PCR: *atp1*^{S178A}, *atp1*^{T185A}, *atp2*^{S35A}, *atp7*^{S109A}, *atp15*^{S34A}, *ald4*$^{3A(S96A,\ S269A,\ S500A)}$. To obtain the triple phosphomutant of *ALD4* – *ald4*^{3A} – plasmid pML767 which contains the *ALD4* gene was subjected to site directed mutagenesis. Three primers coding for S96A, S269A and S500A were used simultaneously, resulting in plasmid pML818. Plasmids pML767 and pML818 were used to reconstitute an *ald4Δ* strain by the integration of the respective linearized vector variant into the promotor region of *ALD4* using SmaI.

Meiotic time courses and cycling cultures

Meiotic time courses were performed with diploid SK1 strains produced by mating the MATa and MATα haploids, as previously described.[26,27] In brief, cells were grown for 2 days at 30 °C on $YP_{2\%Glycerol}$ plates and then amplified as a thin lawn on YPD plates. Cells were used to inoculate pre-sporulation medium $YP_{2\%KAc}$ at OD_{600} = 0.3 and cultured for 11 h (30 °C). Meiotic induction was initiated by switching cells to sporulation medium (SPM, 2% KAc) at OD_{600} = 3.5 – 4. The time of inoculation in SPM was defined as t = 0 h. For MS-sample collection, cultures were upscaled to a 10 L fermenter system as previously described.[85,102,103] Samples were collected at 0 h and from 2–10 h in a 1-hour interval. Cells from mutant backgrounds *ndt80Δ* and *cdc20*^{mn} were collected 8 h or 10 h after transfer to SPM, respectively. Asynchronously cycling cultures were generated by inoculating YPD from an exponentially growing culture to OD_{600} ∼ 0.2. Cells were grown for 2.5 generations and harvested at OD_{600} ∼1.2. Mitotic arrests were achieved by addition of 15 μg/ml nocodazole to cycling cultures and subsequent culturing for 3 h at 30 °C. Cell cycle stage distribution and release from G1 arrest and entry into pre-meiotic S-phase were tracked by analyzing the cellular DNA content on a FACS Canto cell sorter using propidium iodide (55 μg/ml) staining. Meiotic progression was observed by analyzing the kinetics of nuclear division, spindle formation, SC dynamics and spore formation.

FACS analysis of DNA content

Cellular DNA content was determined using a FACS Calibur or FACS Canto cytometer (Becton, Dickinson) running FACSDiva software. Briefly, 1 ml of meiotic culture was collected and fixed in 70% cold ethanol. Cells were washed once and then resuspended in 50 mM Tris-HCl pH 7.5. RNA was digested for min. 4 h at 37 °C (2 μl RNaseA, 100 mg/ml). Cells were washed once in FACS buffer (200 mM Tris-HCl pH 7.5, 211 mM NaCl, 78 mM $MgCl_2$) and sonicated in FACS buffer containing 55 μg/ml propidium iodide. 60 μl of sample in 1 ml 50 mM Tris-HCl pH 7.5 was used to measure DNA content. For each sample > 25'000 cells were analzysed.

Sporulation efficiency assay

A meiotic time course was setup as described above. After switching from $YP_{2\%KAc}$ to 2% KAc cells were left to sporulate for 24 or 48 hours. Samples were collected and analyzed after 24 h or 12 h, 24 h and 48 h (see indications in figure legends). Samples were imaged using a DeltaVision Ultra Epifluorescence Microscope equipped with a 60x 1.4 NA DIC Oil UplanXApo objective, a sCMOS camera under control of Acquire Ultra user interface (version 1.2.3). Ascospores and cells were manually inspected using Fiji[88] imaging software. 200 ascospores or cells were counted in three independent experiments. Ascospore formation was considered successful if they contained at least two spores enclosed by separate spore wall. Statistical analyses were performed using Microsoft Excel and Prism. The results were depicted in Prism.

Spore viability assay

Yeast cells were thawed freshly onto YPD plates and grown for 24 h at 30 °C. Cells were then transferred to SPM-plates and left to sporulate for 24 h. Small amounts of cells were resuspended in Zymolyase 20T in water (1:10 dilution of 1 mg/ml stock) and incubated for 10 min at RT. 20 μl of the cell suspension were transferred onto a YPD plate and individual spores of a tetrad were separately relocated on the YPD plate using a Singer MSM400 Microdissector. Cells were left to grow for 48 h at 30 °C before number of grown

spores was determined. A total of 288 spores were dissected per genotype in four replicates of 72 spores. Statistical analyses were performed using Microsoft Excel and Prism. The results were depicted in Prism.

Yeast spot assay

Cells were grown in YPD O/N at 30 °C to saturation. Cultures were then diluted to OD_{600} = 0,3 and spotted in 4 serial dilutions on YPD or $YP_{2\%Glycerol}$ plates and incubated at 30 °C. Dilution rate: 1:10. Colony growth was assessed 1 or 2 days post spotting.

Immunofluorescence imaging

For yeast whole cell immunofluorescence staining and yeast meiotic chromosome spread staining, published procedures were applied.[98,104,105] Primary antibodies used were rat anti-α-tubulin (1:300, Biorad MCA78G), rabbit anti-Zip1 (1:500, SantaCruz and[85]), mouse anti-mCherry (1:500, Clontech Takara 632543), rabbit anti-Ald4 (1: 1000, this study). Secondary antibodies coupled to Alexa 555, Alexa 488 and Alexa 647 were used for detection (1:300, Invitrogen). DNA was stained with 4',6-diamidino-2-phenylindole (DAPI). Images were acquired on a DeltaVision multiplex (GE healthcare) with a 60x 1.4NA DIC Oil PlanApoN objective or a DeltaVision Ultra epifluorescence microscope (GE Healthcare) with a 100x 1.4NA Oil UPlanSApo objective, using an sCMOS camera controlled by Softworx (version 4.1.0; Applied Precision) or AcquireUltra software (version 1.2.3), respectively. In general, images were modified in Fiji for presentation using linear brightness and contrast adjustments.[88] For Figure S6B, images were deconvolved using Huygens Professional (SVI) and the maximum intensity was z-projected over the area of acquisition in Fiji. For spindle quantification and synaptonemal complex formation >100 cells each were analyzed. Statistical analyses were performed using Microsoft Excel and Prism.

Protein analyses

Samples were processed as described.[47] In short, cell pellets were supplemented with glass beads and disrupted in 10% TCA using a FastPrep-24 (MP Biomedicals) running two cycles of 40 s (6.5 m/s). The protein precipitates were resuspended in 2X NuPAGE sample buffer and neutralized with 1 M TrisBase at a 2:1 ratio, boiled at 95 °C for 10 min and cleared by centrifugation for another 10 min, full speed. Preceding sample loading, concentration was assessed. For nativePAGE, 4 ml of meiotic cultures (OD_{600}=3.5) were supplemented with freshly prepared 2 mM PMSF/DMSO. Cells were harvested and lysed in mild lysis buffer (50 mM Tris-HCl pH=7.5, 25 mM NaCl, 1 mM EDTA pH=8, 0.1% Triton X-100, 100 mM β-glycerophosphate, 20 mM NaF), 1 mM PMSF and protease inhibitor tablets (Roche, 1/50 ml) were freshly added. Cell walls were disrupted using a FastPrep-24 (MP Biomedicals) running two cycles of 40 s (6.5 m/s) with a 5 min break between cycles. Lysates were cleared and adjusted to equal protein concentrations. Samples were then split and either mixed with nativePAGE sample buffer or NuPAGE (denaturing) sample buffer. Denatured samples were boiled at 95 °C for 10 min prior to loading. Native samples were loaded directly.

For immunoprecipitation, 50 ml sample of meiotic cultures (OD_{600}=3.5) were supplemented with PMSF/DMSO 2 mM final upon collection. Cells were lysed in buffer B (50 mM Hepes/KOH pH7.4, 100 mM β-glycerophosphate, 5 mM MgOAc, 0.1% Triton X-100, 10% Glycerol, 20 mM NaF). 1 mM DTT, 1 mM PMSF and protease inhibitor tablets (Roche, 1/50 ml) were freshly added. Lysates were cleared and adjusted to equal protein concentrations. Myc-tagged proteins were captured using anti-Myc agarose beads (9E10, Cancer Research UK) while rotating for 1 h at 4 °C. Agarose beads were split in 4 equal parts for phosphatase treatment after several rounds of washes with increasing salt (2x 70 mM, 1x 150 mM, 1x 200 mM, 2x 70 mM KAc). Phosphatase treatment was carried out using 4 conditions: 1) PMP buffer and $MnCl_2$; 2) PMP buffer and $MnCl_2$; 3) PMP buffer, $MnCl_2$ and λ-phosphatase; 4) PMP buffer, $MnCl_2$ and heat-inactivated λ-phosphatase. Conditions 2-4 were incubated 15 min, 30 °C. Samples were washed twice prior to analysis by western blotting.

Denatured protein samples were separated on NuPAGE 3-8% Tris-Acetate (Invitrogen) or NuPAGE 4-12% Bis-Tris gels using matching running buffers. For Phostag gels 7% acrylamide gels were supplemented with 20 μM PhosTag™ and 10 mmol/L $MnCl_2$. NativePAGE was carried out using NativePAGE 4-16% Bis-Tris gels and nativePAGE running buffer (Invitrogen). Proteins were transferred onto Amersham Hybond 0.45 μm PVDF membranes. Phostag gels were washed 3x 5 min in transfer buffer containing 10 mM EDTA prior to transfer. For nativePAGE, marker lanes were cut prior to antibody incubation for staining with Coomassie. For immunoblotting the following antibodies were used: mouse anti-Myc HRP conjugated (1:15000, ab1326 Abcam), mouse anti-FLAG HRP conjugated (1:10000, A8592-1MG Sigma Aldrich), mouse anti-GFP (1:2000, 11814460001 Roche), mouse anti-Cdc5 (1:2500, MM-0192-1-100 MédiMabs), rabbit anti-Crm1 (1:5000, [83]), rabbit anti-Puf6 (1:5000, [84]), rabbit anti-Ald4 (1:2000, this study). The following secondary antibodies were used: 1:5000 goat anti-mouse immunoglobulin conjugated to HRP (P0447 Agilent) and 1:5000 swine anti rabbit immunoglobulin HRP conjugated (P0339 Agilent).

MS data acquisition and analysis

Sample preparation, as described in King et al.[21] In short, 100 ml samples from a meiotic time course were collected per time point and supplemented with 100% Trichloroacetic acid (TCA) to a final concentration of 6.25% on ice. Samples were washed twice with cold acetone and pellets were snap frozen in liquid nitrogen. Proteins were extracted in 400 μl lysis buffer (8 M urea, 100 mM ammonium bicarbonate, 5 mM EDTA, pH = 8) in combination with glass beads and in batches of 12. Extraction step was repeated 5 times with fresh lysis buffer. Protein concentration was assessed with BCA (Pierce) and 3 mg of total protein was used for downstream processing. Samples were sequentially incubated with 5 mM TCEP (1 h, 25 °C), 12 mM Iodoacetamide (1 h, 25 °C, dark), then diluted 8 times with 100 mM ammonium bicarbonate (reducing urea to 1 M) and finally trypsin digested ON, 37 °C (trypsin:protein ratio 1:100).

Prior to peptide enrichment on C18 silica reversed-phase chromatography column (Sep-Pak C18 3cc, Waters) samples were acidified to pH ~2.5 with formic acid (FA). Peptides were eluted in 50% acetonitrile (ACN), 0.1% FA, speedvac-dried and reconstituted in 50 µl 0.1% FA. For the total proteome assessment ("unenriched"), 1 µl was diluted to 1 µg/µl. The remaining sample was diluted with a 1.14x lactic acid solution (5 ml ACN, 2.92 ml lactic acid, 20 µl 50% TFA, filled with H_2O to 8.7 ml) and used for phosphopeptide enrichment by TiO_2 affinity purification.

Samples were incubated 1 h RT on a rotator with TiO_2 resin (GL Science) pre-equilibrated with 1X lactic acid solution. Beads were washed sequentially with lactic acid, 80% ACN 0.1% TFA and 0.1% TFA. Phosphopeptides were eluted in 50 mM ammonium phosphate pH = 10.8 and acidified to pH = 2 by adding 50% FA. Samples were concentrated on C18 Micro Spin Columns (The Nest group), eluted in 50% ACN, 0.1% FA, speedvac-dried and resuspended in 0.1% FA. All samples were spiked with iRT reference peptides (Biognosys) for reference.

Mass spectrometry data acquisition

1 µg of peptides were injected either on a 5600 (unenriched datasets) or 6600 (phospho-enriched datasets) Sciex TripleTOF mass spectrometer with an Eksigent NanoLC Ultra 1D Plus system interface. The peptides were separated on a 75-µm-diameter, 20 cm-long new Objective emitter packed with Magic C18 AQ 3 µm resin (Michrom BioResources) and eluted at 300 nl/min with a linear gradient of 5-to-35% Buffer A for 120 min (Buffer A: 2% acetonitrile, 0.1% formic acid; Buffer B: 98% acetonitrile, 0.1% formic acid). MS data acquisition for the individual samples was performed in data-independent acquisition (DIA) SWATH MS mode using 32 fixed precursor isolation windows of 25 Da width (+1 Da overlap) acquired each for 100 ms plus one MS1 scan acquired for 250 ms as described in Gillet et al.[32] MS data acquisition of the pooled samples for library generation was performed in data-dependent acquisition mode (DDA, top20, with 20 s dynamic exclusion after 1 MS/MS). For either mode, the mass ranges recorded were 360-1460 m/z for MS1 and 50-2000 m/z for MS2 and the collision energy was set to 0.0625 × m/z - 6.5 with a 15-eV collision energy spread regardless of the precursor charge state. Library samples consist of the following triplicate pools of individual timepoints: t = 0 h and 2 h; t = 3 h, 4 h, 5 h; t = 6 h and 7 h; t = 8 h, 9 h, 10 h; *ndt80Δ* arrest; *cdc20*^{mn} arrest and mitotic and cycling samples.

DDA data analysis

The DDA search and spectral library generation were done as described in Schubert et al.[33] In short, the raw DDA files were converted to mzXML using msconvert (Proteowizzard v 3.0.9987). The converted files were searched with Comet (2014.02 rev. 0) and Mascot (version 2.5.1) using the yeast SGD database (release 13.01.2015) appended with the SK1 and W303 entries (for a total of containing 12'036 proteins plus one protein entry for the concatenated sequence of the iRT peptides and as many decoy protein entries generated by pseudo-reversing the tryptic peptide sequences). The following parameters were selected for the search: +/- 25 ppm tolerance for MS1 and MS2, fixed cysteine carbamidomethylation, either variable methionine oxidation (for the unenriched datasets) or variable methionine oxidation and variable serine/threonine/tyrosine phosphorylation (for the phospho-enriched datasets), semi-tryptic and 2 missed cleavages allowed. The output from comet and mascot search was further processed using peptideProphet[106] and aggregated using iProphet[107] (TPP v4.7 rev 0). The cutoff in iProphet was set at 1% false discovery rate. For the phospho-enriched datasets, the confidence of phosphorylation site localization was assessed using LuciPhor. Two consensus spectral libraries were generated using[108] depending on the confidence in phosphorylation-site localization and the two assay libraries thereof were exported using the spectrast2tsv.py script[33] with the following parameters: 5 highest intensity fragments (of charge 1+ or 2+) per peptide, within the mass range 350-2000 m/z, allowing fragments with -79.97 or -97.98 neutral losses, and excluding the fragments within the precursor isolation window of the corresponding swath. The final library retained in priority assays from the high confidence localization and then the assays from the low confidence localization. The assay library was finally exported to TraML with shuffled decoys appended as described in Schubert et al.[33]

SWATH MS targeted data extraction and data filtering

The SWATH MS data was extracted based on the above generated assay library through the iPortal interface with openSWATH[89] (openMS 2.1.0), pyProphet[90] and TRIC alignment[89] using the same parameters as described in Navarro et al.[109] Further processing was done in R – for the initial steps similar as described in King et al.[21] The precursor intensities were first log_2-transformed and normalized (mean-centering). Assays identifications were filtered for detection in two out of three triplicates for at least one condition. The missing values were imputed at the precursor level using either a random value amongst a distribution centered at the mean of the other replicate values of that triplicate series (when at least 1 value was found for that triplicate) or centered on a value 3-fold lower than the lowest value of that precursor, and with a standard deviation equal to the mean standard deviation of all the replicate precursor values. For the unenriched dataset all the precursor intensities summed to a protein intensity value for the unenriched datasets. The consequent analysis was done either on the protein level (unenriched dataset), or on the precursor level (phospho-enriched dataset), or on the "corrected phospho-stoichiometry" level. For that last level, the overall fold-change in phosphorylation for each precursor compared to time point 0, was divided by the corresponding fold-change in the protein abundance compared to time point 0. Statistical significance was assessed by ANOVA across the all dataset, for either of the three levels mentioned above and species with a corrected *p* value of 0.01 and a fold change above 2 compared to the mean value across the dataset were used for further fuzzy clustering analysis and heatmap plotting.[38]

Venn-Diagrams and GO-analyses in Figures 1, S2, and S6: For the generation of Venn diagrams the Venny 2.1 online tool was used (https://bioinfogp.cnb.csic.es/tools/venny/). The BioGRID repository BIOGRID_PTMS-3.5.180ptm[28,36] were used for global dataset comparisons. Phosphorylation reported on histidine were omitted. For GO-term analysis, the DAVID online tool was used.[110] The total proteome recorded or the phosphoproteome were used as background respectively. Results were corrected for multiple comparisons. Top 5 hits were chosen.

For data analysis in Figures 2H, 4A, 5A, and S3A the phosphopeptides reported in this study were annotated using the yeast genome release S288C_reference_genome_R64-2-1_20150113.[111] The raw intensities of the phosphorylated peptides were normalized to obtain distributions with the same median across samples. For the analysis of changing phosphorylation levels of protein peptides during the vegetative growing cells and the meiosis time course, the normalized intensities of the three replicates per condition were averaged and compared to the mean of each phosphopeptide expression level divided by their standard deviation across all the cellular contexts, thus transforming the phosphorylation intensities into Z-scores. Additionally, individual phosphosites present in multi-phosphorylated peptides were split into single phosphosites and their quantifications were retained for further analysis if they were not part of the set of mono-phosphorylated peptides.

Statistical analysis and data visualization

The data processing performed and all statistical methods were implemented using R 3.5.1 (“The R Project for Statistical Computing” n.d.). The visualization of heatmaps was done with the ComplexHeatmap R package version 2.0.0.[91]

Gene Ontology Enrichment Analysis

Gene Ontology enrichments of biological processes were estimated with a Z-test method that compares the mean Z-scores of all phosphorylated proteins belonging to a given GO term against the mean and variance of all Z-scores quantified in a given condition. Only GO terms with a minimum of 12 phosphosites from at least 4 different proteins (mean value of proteins annotated to yeast GO terms) were considered. Unique phosphopeptide isoforms were used as input. The GO enrichment scores (ES) were estimated using the $-\log_{10}$(p value) of the Z-test and they were signed based on the mean Z-score of all phosphorylated proteins from a GO term. GO terms having an enrichment score (abs(log10(p value) >=2 in at least one condition were determined to undergo significant phosphoregulation. The same methodology was applied to the unenriched dataset. The list of GO terms was obtained from the Ensembl database (version 86),[86] using the biomaRt R package version 2.38.0.[92]

Phosphoregulation of the yeast kinome and protein complexes

Known kinase-substrate interactions from yeast were obtained from BioGRID[87] excluding studies with indirect evidence for kinase-substrate interactions.[112] The yeast protein complexes were downloaded from the oak lab website (http://wodaklab.org/cyc2008/). This collection includes 408 heteromeric protein complexes supported by small-scale experiments curated from the literature.[45] The phosphoproteome mapped to the known kinase-substrate interactions and the protein complexes was used to estimate kinase activities (with at least 3 quantified substrates) and the phosphoregulation of the protein complexes using the Z-test method benchmarked in Hernandez-Armenta et al.,[37] respectively.

Phosphosite motif enrichment was performed by comparing unique phosphosite sequences within each cluster to the entire quantified phosphoproteome using the R package DagLogo.[93] Significantly enriched amino acids (Fisher’s exact test $p < 0.05$) were visualized with the R package ggseqlogo.[94]

Removing redundancy in functional analyses

To prevent redundant GO terms, kinases and protein complexes, we calculated the pairwise distance between each of these functional groups using the metric: 1-Jaccard Similarity Coefficients of shared genes present in the phosphoproteome, with this distance we constructed three different hierarchical clusterings. Each tree was cut at a height of 0.99, and we selected the GO terms/Kinases/Protein Complexes with the highest number of unique proteins per cluster.

Mitochondria isolation

A small-scale mitochondria isolation protocol was used as described previously.[64] Briefly, ~350 OD_{600} units of meiotic yeast cell culture were harvested, washed in water, and incubated in 100 mM Tris-SO_4 pH 9.4 containing 10 mM DTT for 20 min at 30 °C. Cells were washed in zymolyase buffer (1.2 M sorbitol, 20 mM KP_i pH 7.4) and incubated in 1.5 ml zymolyase buffer containing 10 mg 20T zymolyase (Seikagaku Biobusiness) for 30 min at 30 °C. After cell wall digestion, spheroplasts were washed in zymolyase buffer and resuspended in homogenization buffer [0.6 M sorbitol, 10 mM Tris/HCl pH 7.4, 1 mM ethylenediaminetetraacetic acid (EDTA), 2 mM phenylmethylsulfonyl fluoride (PMSF), 0.2% (w/v) bovine serum albumin]. Spheroplasts were homogenized by passing the cell suspension 20 times through a 0.8 × 22 mm cannula. The suspension was centrifuged at 1,000 × *g* to remove nuclei and cell debris and the crude mitochondrial fraction was isolated by centrifuging the supernatant at 12,000 × *g* for 15 min. Mitochondria were resuspended in SEM buffer (250 mM sucrose, 1 mM EDTA, 10 mM MOPS/KOH pH 7.2) and the protein concentration was estimated against an Albumin standard by the Bradford method. Aliquots were directly used for plunge-freezing.

Plunge-freezing

Yeast cells were cultured as described above and plunge-frozen as described before[62] with minor modifications. Meiotic yeast cells or spores were harvested and diluted to an OD_{600} of 1-3 in SPM. Vegetatively growing cells (asynchronously proliferating cultures in YPD) were harvested at an OD_{600} of ~0.8, spinned for 2 min at 650 x *g* and resuspended in SPM to OD_{600} of 1-3. Yeast cells or spores were kept on ice until they were plunge-frozen with a Vitrobot Mark IV (Thermo Fisher Scientific).[113] 4 μl of cell suspension was pipetted onto negatively glow-discharged EM grids (R2/2 Cu200 mesh, specially treated, Quantifoil). Grids were back-blotted using a Teflon sheet on one side either once for 5 - 6 s or twice for 3 - 5 s at 4 °C, 95% humidity, before plunging them into liquid ethane/propane mixture [37% (v/v) ethane].[114] Isolated mitochondria were mixed with 10 nm BSA-coated colloidal gold particles (Cytodiagnostics) in a ratio of 5:1 before 3 μl of sample was applied onto negatively glow-discharged EM grids (R2/2 Cu 200 mesh, specially treated, Quantifoil). Grids were back-blotted for 5 s at 4 °C, 95% humidity and were plunge-frozen.

CryoFIB milling

Prior to cryoET, plunge frozen cells or spores were cryoFIB-milled with a Crossbeam 550 FIB-SEM instrument (Zeiss) as described before.[62] The FIB-SEM instrument was equipped with a copper band-cooled mechanical cryo-stage (Zeiss), an SE2 detector (Zeiss), an in-lens secondary electron detector (Zeiss), and an integrated VCT500 vacuum transfer system (Leica Microsystems). Briefly, after plunge-freezing, EM grids were clipped into FIB milling Autogrids (Thermo Fisher Scientific) and loaded onto a cryoFIB Autogrid holder[115] (Leica Microsystems) using a VCM loading station (Leica Microsystems). The Autogrid holder was transferred to an ACE600 (Leica Microsystems) with a VCT500 shuttle and the sample was cryo-sputter coated with a 4 nm thick layer of tungsten. After loading the sample into the Crossbeam 550, grids were additionally coated with organoplatinum and automated sequential FIB milling was set up. A pattern with four currents was used (rough milling: 700 pA, 300 pA and 100 pA; polishing: 50 pA) to mill ~300 nm thick lamellae. After milling, samples were transferred back to the VCM loading station with the VCT500 shuttle for unloading and grids were stored in liquid nitrogen until cryoET imaging.

CryoET data collection and processing

CryoET data were collected on Titan Krios transmission electron microscopes (TEM) (Thermo Fisher Scientific) operating at 300 kV and equipped with Quantum LS imaging filters (slit width 20 eV) (Gatan) and either K2 (Krios1) or K3 (Krios2) direct electron detectors (Gatan) or equipped with BioContinuum imaging filter and K3 direct electron detectors (Gatan) (Krios3). Low magnification overviews were collected in SerialEM[95] for navigation and targets were selected for the following tilt series collection. For lamella, a bidirectional tilt series collection scheme was used with an angular range between ±70° to ±50°, depending on the lamella pre-tilt, with 2° increments and a defocus of -8 μm. The total dose per tilt series accumulated ~120 $e^-/Å^2$ and the pixel sizes were 4.34 Å/pixel (Krios 1) or 4.57 Å/pixel (Krios 2) at specimen levels. For purified mitochondria, tilt series were collected using a bidirectional scheme with an angular range between +60° to -60°, with 3° increments and a defocus of -8 μm. The pixel size was 2.68 Å/pixel (Krios3) at the specimen level and the total dose per tilt series accumulated ~160 $e^-/Å^2$.

Frames were aligned using 'alignframes' and tomograms were reconstructed subsequently in IMOD.[96] Cryo-tomograms shown in the figures were binned at the level of 4 and filtered using 'tom_deconv'.[116] Cryo-tomogram segmentations were manually performed in IMOD.

Mitochondrial ultrastructure analysis

Cryo-tomograms of FIB-milled yeast cells or spores containing mitochondria were manually inspected in IMOD. Overall mitochondrial area and mitochondrial inter-membrane space (IMS) were measured manually using the "Sculpt" drawing tool in IMOD. Only mitochondria with a continuous double-membrane visible in one tomogram slice were counted for the measurements. The presence of filamentous assemblies was checked for individual mitochondrial cross-sections within cryo-tomograms. Filament assemblies were counted if they looked like "spherical particle clusters" or parallel filaments based on their orientation within the cryo-tomogram. Data analysis was performed in Excel and Prism software.

The figures containing the structure of Ald4 were visualized using UCSF ChimeraX.[97]

QUANTIFICATION AND STATISTICAL ANALYSIS

Statistical analyses were performed using Microsoft Excel, Prism or RStudio. For multiple comparisons, analysis of variance (one-way ANOVA) was performed with Prism, followed by a correction for multiple comparisons using statistical hypothesis testing (Dunnett test). For pairwise comparisons two-tailed unpaired t-tests were used. The *p* value for the difference between the logarithmized wild type counts and the logarithmized counts for a given mutant serves as an indication for a significant difference in counts. Detailed descriptions can be found in each section of the respective experimental method.